Check for updates

JGR Space Physics

RESEARCH ARTICLE
10.1029/2021JA029363

Key Points:

- Each of 37 high-energy electron flux enhancement events began at $L > 4$
- Ultra Low Frequency wave activity localized in L is decisive to the position of the high-energy electron flux enhancement pattern ($L > 4$)
- Each event occurred during High-Speed Stream in conjunction with Alfvénic fluctuations, Bz southward, substorms and chorus/ULF waves

Supporting Information:

Supporting Information may be found in the online version of this article.

Correspondence to:

L. A. Da Silva,
ligia.alves01@gmail.com;
ligia.silva@inpe.br

Citation:

Da Silva, L. A., Shi, J., Alves, L. R., Sibeck, D., Marchezi, J. P., Medeiros, C., et al. (2021). High-energy electron flux enhancement pattern in the outer radiation belt in response to the Alfvénic fluctuations within High-Speed solar wind stream: A statistical analysis. *Journal of Geophysical Research: Space Physics*, *126*, e2021JA029363. https://doi.org/10.1029/2021JA029363

Received 19 MAR 2021
Accepted 21 JUL 2021

© 2021. American Geophysical Union. All Rights Reserved.

High-Energy Electron Flux Enhancement Pattern in the Outer Radiation Belt in Response to the Alfvénic Fluctuations Within High-Speed Solar Wind Stream: A Statistical Analysis

L. A. Da Silva[1,2], J. Shi[1], L. R. Alves[2], D. Sibeck[3], J. P. Marchezi[1,2], C. Medeiros[2], L. E. A. Vieira[2], O. Agapitov[4], F. R. Cardoso[5], V. M. Souza[2], A. Dal Lago[2], P. R. Jauer[1,2], C. Wang[1], H. Li[1], Z. Liu[1], M. V. Alves[2], and M. S. Rockenbach[2]

[1]State Key Laboratory of Space Weather, National Space Science Center, Chinese Academy of Sciences, Beijing, China, [2]National Institute for Space Research – INPE, São José dos Campos, Brazil, [3]NASA Goddard Space Flight Center, Greenbelt, MD, USA, [4]Berkeley - UCB - Space Sciences Laboratory, University of California, Berkeley, CA, USA, [5]Lorena School of Engineering (EEL), University of São Paulo - USP, Lorena, Brazil

Abstract The coupling response between solar wind structures and the magnetosphere is highly complex, leading to different effects in the outer radiation belt electron fluxes. Most Coronal Mass Ejections cause strong geomagnetic storms with short recovery phases, often 1–2 days. By contrast, High-Speed Solar Wind Streams lead to moderate and weak storms often with much longer recovery phases, from several to ∼10 days. The magnetosphere receives energy for a long time under the influence of the HSSs, considerably changing its dynamics. This in turn has an effect on the charged particles trapped in the outer radiation belt. Although the high-energy electron flux enhancements have received considerable attention, the high-energy electron flux enhancement pattern ($L > 4$) has not. This paper identifies 37 events with this enhancement pattern in the high-energy electron flux during the Van Allen Probes era. We find the enhancements coincident with HSS occurrence. The interplanetary magnetic field (IMF) exhibits north/south Bz fluctuations of Alfvénic nature with moderate amplitudes. The high-energy electron flux enhancements also correspond to long periods of auroral activity indicating a relationship to magnetotail dynamics. However, the AE index only reaches moderate values. Ultra-Low Frequency waves were present in all of the events and whistler-mode chorus waves were present in 89.1% of the events, providing a convenient scenario for wave-particle interactions. The radial gradient of the ULF wave power related to the L, under the influence of the HSSs, is necessary to trigger the physical processes responsible for this type of high-energy electron flux enhancement pattern.

1. Introduction

The coupling response between the solar wind structures and the magnetosphere is generally studied regarding the geomagnetic storm phases (Burlaga & Lepping, 1977; Echer et al., 2008; Gonzalez et al., 1999; Richardson & Cane, 2012). The majority of strong geomagnetic storms (Dst ≤ −100 nT) are driven by coronal mass ejection (CME), with a short recovery phase, typically a couple of days (e.g., Echer et al., 2008; Tsurutani & Gonzalez, 1997). In contrast, high-speed solar wind streams (HSS) lead to moderate and weak long lasting storm recovery phases, that is, from a few to ∼10 days (Richardson et al., 2006; Tsurutani et al., 1995). Consequently, they may deposit more energy in the magnetosphere compared to the larger CME-driven storms (Miyoshi & Kataoka, 2005; Turner et al., 2006).

Alfvénic fluctuations in the interplanetary magnetic field are commonly observed during the long recovery phases of the HSS (Da Silva et al., 2019; Tsurutani et al., 1995). This behavior is generally concomitant with moderate substorms activities, in which intermittent intervals of enhanced magnetospheric convection can inject low-energy particles into the outer radiation belt (Forsyth et al., 2016; Lyons et al., 2009). The low-energy (1–20 keV) particles injection leads to generation of whistler-mode chorus waves (hundreds of Hz up to about 10 kHz) (e.g., Gurnett & O'Brien, 1964; Miyoshi et al., 2007). Chorus waves play an essential role in the local acceleration of medium-energy electrons (<100 keV) up to relativistic levels in the outer

radiation belt through the energy diffusion (Jaynes et al., 2015, 2018; Shprits & Ni, 2009; Xiao et al., 2010; Zhao et al., 2018).

Substorms associated with HSS can also contribute to the production of Ultra Low Frequency - ULF waves (a few millihertz up to about 5 Hz) (e.g., Claudepierre et al., 2008; Elkington, 2006; Elkington et al., 1999; Kavosi & Raeder, 2015; Kivelson & Southwood, 1985; Mann et al., 1999) through energy deposition (James et al., 2016, 2013; Yeoman et al., 2010). HSSs' energy transfer to the magnetosphere via Kelvin-Helmholtz instabilities can lead to the generation of the ULF waves, which also have an essential role in accelerating medium-energy electrons up to high-energies (i.e., relativistic) through inward radial diffusion (Da Silva et al., 2019; Jaynes et al., 2018; Souza et al., 2017; Zhao et al., 2018).

Although the global recovery of the outer radiation belt under the influence of the HSS has been widely studied in the last few decades (Da Silva et al., 2019; Hartley et al., 2013; Jaynes et al., 2015; Miyoshi et al., 2013; Souza et al., 2017); a poor understanding remains regarding the different high-energy electron flux enhancement patterns in the outer radiation belt and their associated generation mechanisms. This paper presents the statistical results of the high-energy electron flux enhancements indicating that the enhancements start at $L > 4$ in response to the Alfvénic fluctuations within HSS, and after that remains displaced without flux enhancement below $L \leq 4$.

2. Data Set and Methodology

The relativistic Electron-Proton Telescope (REPT, Baker et al., 2013), Magnetic Electron Ion Spectrometer (MagEIS, Blake et al., 2013) and Helium, Oxygen, Proton, and Electron (HOPE, Funsten et al., 2013) instruments onboard of the Van Allen Probes (Mauk et al., 2012) provide the electron flux in the respective channels, 1.8–23 MeV, 33–4,062 keV and 14.98–51,767 eV. The Magnetic Field Experiment (MAG) and Solar Wind Electron, Proton, and Alpha Monitor (SWEPAM) onboard the Advanced Composition Explorer (ACE, Stone et al., 1998) satellite provides the solar wind parameters at the L1 Lagrangian point. DONKI repository (Database of Notifications, Knowledge, Information) available at https://kauai.ccmc.gsfc.nasa.gov/DONKI/search/ is used to confirm the type of the solar wind structures. The auroral electroject (AE) index with a 5-min averaged average time cadence is obtained at OMNIWeb (https://omniweb.gsfc.nasa.gov/).

Whistler-mode chorus wave power measured are provided by the Electric and Magnetic Field Instrument Suite and Integrated Science (EMFISIS) (Kletzing et al., 2013) and Electric Field and Waves (EFW) (Wygant et al., 2013) instruments onboard of the Van Allen Probes (one spectrum every 5 s). The chorus wave detection in this work is limited to in situ observations in the outer radiation belt using the Van Allen Probes data. A more complete view of the global chorus wave activity could possibly be achieved by employing a proxy such as shown in Chen et al. (2014), but this is outside the scope of this paper. ULF wave powers are estimated making use of the data from the International Monitor for Auroral Geomagnetic Effects (IMAGE) ground magnetometer network in Scandinavia (Viljanen & Hakkinen, 1997) and the EMFISIS.

Although several Earth's radiation belts missions have provided (and some continue to provide) the high-energy electron fluxes in the outer radiation belt in the last decades, the details of the physical processes leading to high-energy electron flux sudden enhancement are still not fully understood. The high-energy electron flux enhancement under the influence of the HSS has been widely studied (e.g., Baker et al., 1986; Da Silva et al., 2019; Turner et al., 2006). However, the specific high-energy electron flux enhancement pattern, in particular the preferential recovery in the outer or inner boundary of the outer radiation belt, has never been discussed before. Thereby, the focus here is on the preferential global recovery of the electron flux in the outer radiation belt at $L > 4$, named here as high-energy electron flux enhancement pattern.

The scientific community generally uses the storm's intensity as the criterion to select the events to study (see Turner et al., 2019). Here, a visual analysis of high-energy electron flux during the Van Allen probes era (2013–2018) is the first approach applied to select the events in the study. The high-energy electron flux enhancements at 2.10 MeV were concentrated around the L-shell ~5.0 and they were observed after a slight flux decrease. These events were selected, as presented in Figures S38–S74 and available at https://rbspgway.jhuapl.edu/. A total of 37 events is selected. It is essential to highlight that the high-energy electron flux

enhancements for these 37 events occurred at $L > 4$. After this preliminary analysis, we classified these 37 events as the high-energy electron flux enhancement pattern.

The interplanetary medium parameters measured at the L1 Lagrangian point are analyzed for each selected event, in which the kind of solar wind structure is identified. Curiously, the high-energy electron flux enhancement pattern observed here in the 37 events is similar to some of the case studies published in the literature (see Da Silva et al., 2019; Jaynes et al., 2015; Souza et al., 2017), that are coincident with the occurrences of HSSs, specifically during the Alfvénic fluctuations period. Thereby, the methodology applied here will be consistent with the approaches discussed by those authors. Therefore, the interplanetary medium conditions, magnetospheric waves, and IMF's Alfvénic fluctuations will be analyzed to identify the likely mechanisms responsible for this high-energy electron flux enhancement pattern.

Each case study (1 and 2) will be analyzed in detail regarding the physical processes responsible for the high-energy electron flux enhancements. Thereby, the solar wind structures' signature will be identified through the solar wind parameters and confirmed through the DONKI repository. Whistler-mode chorus and ULF wave power spectral densities will be analyzed during the high-energy electron flux enhancement pattern. IMF conditions and AE index will be used to identify the concomitances between the Alfvénic fluctuations and the substorms. The main dynamic mechanisms will be investigated to identify the responsible process for this specific electron flux enhancement pattern.

Superposed epoch analysis (SEA) is a widely used technique to identify whether a given type of event may have influenced a physical process that is, either intrinsically random or their measurements are governed by random noise (Jamison & Regal, 1979). Thereby, it is usual to find the studies in the literature regarding the relationship between the solar wind parameters, electron fluxes, and wave activity (e.g., Kalliokoski et al., 2020; Kilpua et al., 2015, 2013; Murphy et al., 2018; Turner et al., 2019). Following this idea, we will use the SEA in this work to obtain the average behavior of the variation in both the high-energy electron flux (2.10 MeV), the interplanetary parameters, the AE index and the ULF wave activity of the 37 selected events.

The first procedure used to apply Superposed Epoch Analysis consists of determining the average variation of the high-energy electron flux (2.10 MeV) for these 37 selected events at $L = 5.0$, $L = 4.5$, and $L = 4.0$. The time series is obtained, and the zero epoch can be defined for the epoch overlap analysis. Although the intensity of the storm is generally used as the criterion to define the zero epoch (e.g., Murphy et al., 2018; Turner et al., 2019), the zero epoch is defined here at the minimum electron flux value observed before the electron flux enhancement pattern (Marchezi, 2020). After the zero epoch is defined for the epoch overlap analysis ($L = 5.0$), the Superposed Epoch Analysis is again used to determine the average variation of both the interplanetary parameters, the AE index and ULF wave power.

3. Results

3.1. Case Studies

3.1.1. High-Energy Electron Flux Pattern Versus Interplanetary Medium Conditions

Figures 1 and 2 show two case studies, respectively, selected through the criteria established in the methodology (enhancement starts at $L > 4$). The physical processes responsible for the high-energy electron flux enhancements pattern are analyzed in detail. Case study 1 occurred on February 28–March 03, 2013 (Figure 1) and case study 2 occurred on March 06–09, 2016 (Figure 2). Panels (a) present the high-energy electron flux (2.10 MeV) for both case studies, in which the pattern of the global recovery seems to be shifted to high L-star compared to the electron population at the beginning time of each event in the study. Panels (b), (c) and (d) present energy electron flux in 1.8 MeV, 2.10 MeV, 2.6 MeV and 3.4 MeV energy channel at a fixed $L = 5.0$, $L = 4.5$ and $L = 4.0$ location, respectively. The high-energy electron flux increase by more than one order of magnitude at $L = 5.0$, increases by approximately one order of magnitude at $L = 4.5$, and increases in less than one order of magnitude at $L = 4.0$ within 12 h. This pattern was observed in each of the 37 events and it means that it is very important to know the main physical processes regarding this electron enhancement pattern to identify whether there is a pattern in the physical processes.

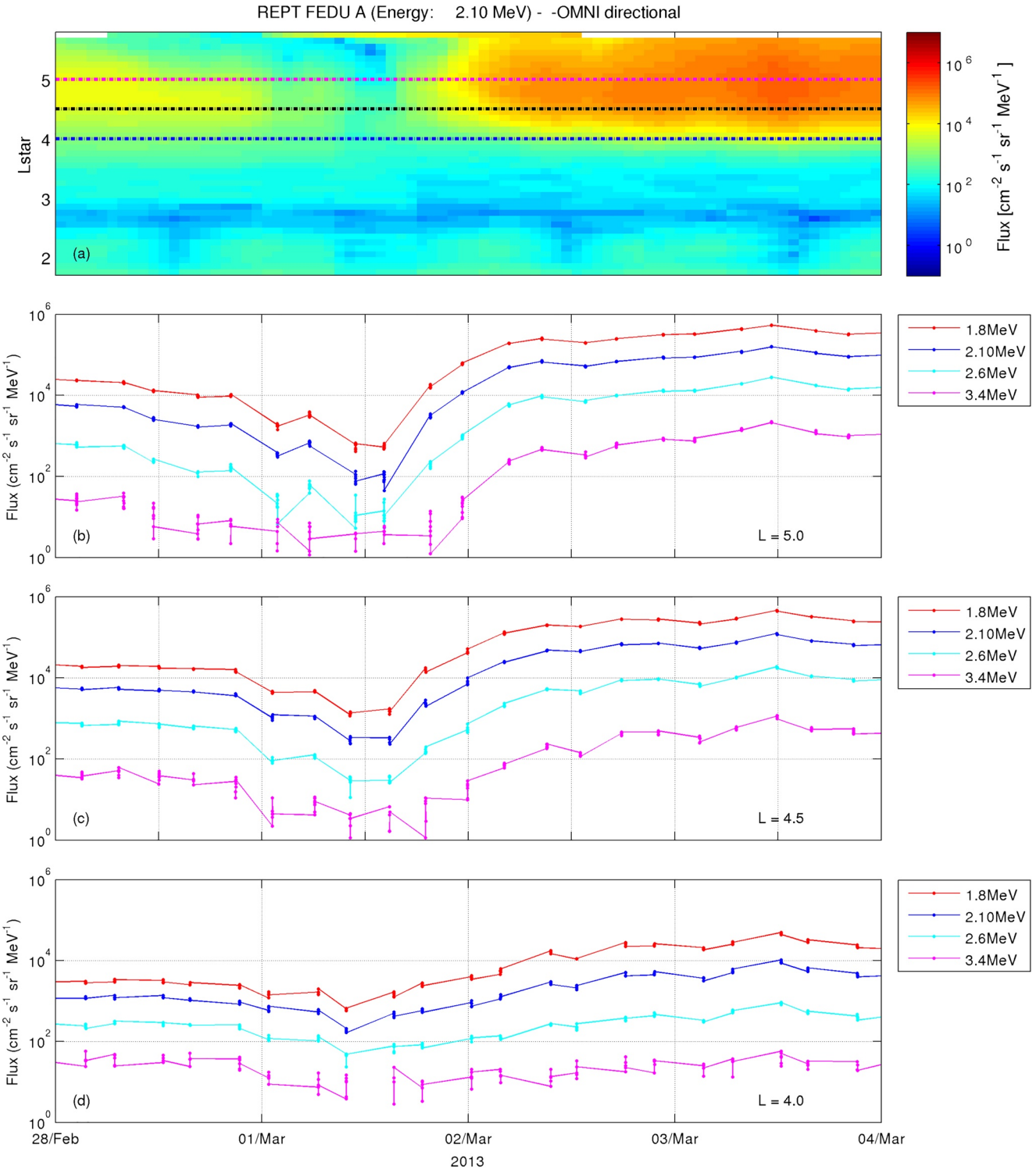

Figure 1. (a) Electron flux at 2.60 MeV energy as a function of L (vertical axis) and time (horizontal axis); (b) electron fluxes at 1.8 , 2.10, 2.6, and 3.4 MeV energies at a fixed $L = 5.0$ location; (c) electron fluxes at 1.8, 2.10, 2.6, and 3.4 MeV energies at a fixed $L = 4.5$ location; (d) electron fluxes at 1.8, 2.10, 2.6, and 3.4 MeV energies at a fixed $L = 4.0$ location. The electron fluxes are obtained by the REPT instrument onboard of the Van Allen Probe A. Case study 1 occurred on February 28–March 03, 2013.

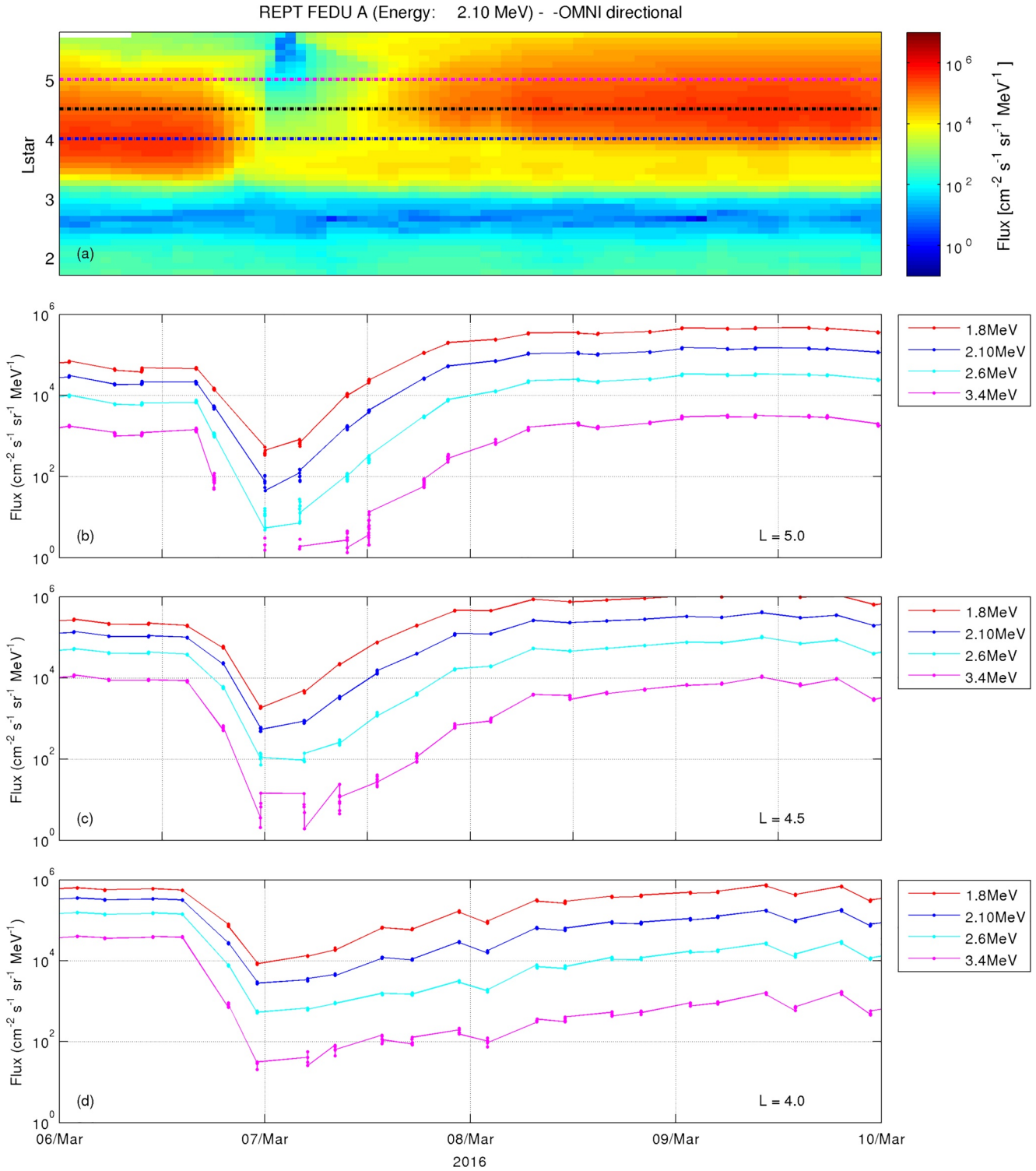

Figure 2. (a) Electron flux at 2.60 MeV energy as a function of L (vertical axis) and time (horizontal axis); (b) electron fluxes at 1.8, 2.10, 2.6, and 3.4 MeV energies at a fixed $L = 5.0$ location; (c) electron fluxes at 1.8, 2.10, 2.6 , and 3.4 MeV energies at a fixed $L = 4.5$ location; (d) electron fluxes at 1.8, 2.10, 2.6, and 3.4 MeV energies at a fixed $L = 4.0$ location. The electron fluxes are obtained by the relativistic Electron-Proton Telescope instrument onboard of the Van Allen Probe A. Case study 2 occurred on March 06–09, 2016.

Figures 3 and 4 show the high-energy electron flux and interplanetary medium conditions and AE index for both case studies, February 28–March 03, 2013 (Figure 3) and March 06–09, 2016 (Figure 4). Panels (a) present high-energy electron flux (2.10 MeV), panels (b) present energy electron flux in 1.8, 2.10, 2.6, and 3.4 MeV energy channel at a fixed $L = 5.0$ location, in which electron flux enhancements are observed at all channels, as discussed before. Panels (c-f) present the interplanetary medium parameters, such as solar wind speed, solar wind density, Bx and By component of the Interplanetary Magnetic Field (IMF), IMF intensity (Bt) and Bz component of the IMF, respectively.

Solar wind speed (Panels [c]) and density (Panels [d]) present the signatures of the High Speed solar wind Stream (HSS) at Lagrangian point L1 for both events. These HSSs reached the Earth's magnetosphere on February 28, 2013, at ∼15:47 UT, and on March 06, 2016, at ∼09:49 UT. These times were estimated through the "flat time-shift" method, in which the solar wind large-scale planar structures are represented by phase planes with normal directed toward the Earth (Cameron & Jackel, 2016). The maximum values of the solar wind speed (Panels [c]) reached ∼600 km/s in both events and they are coincident with the beginning of the high-energy electron flux enhancements observed in Panels (b). During the entire duration of the electron flux enhancements in both events, the densities are smaller than 5 cm^{-3} (panel [d]) and the Bz component oscillates around zero, on average southward oriented (panel [f]).

The fluctuations observed in the Bx, By and Bz component of the IMF (Panels [e] and [f]) suggest the presence of Alfvénic fluctuations associated to HSS during the electron flux enhancements in both events (Figures S1 and S14). The linear correlation between the variation of the solar wind velocity components at L1 Lagrangian point (ACE data) versus the corresponding Alfvén velocity components confirm that these fluctuations observed in (Panel [e] and [f]) are mostly Alfvénic in nature. The linear correlation coefficients for the X, Y, and Z components of the solar wind velocity on March 03, 2013, acquired during a 5-h time interval starting at 10:00 are 0.840, 0.621, 0.901, respectively; and on March 09, 2016 (from 05:00 to 10:00 UT) are 0.614, 0.609, 0.679, respectively (Figures S1 and S14). According to Gonzalez et al. (1994), the Alfvénic fluctuations may provide prolonged intervals of southward Bz, which can initiate the reconnection at the Earth's dayside magnetopause and drive moderate-intensity geomagnetic storms (Tsurutani et al., 1995), as well drive recurrent substorms as observed in Da Silva et al. (2019), Jaynes et al. (2015), and Souza et al. (2017).

AE index (Panels (g)) during the high-energy electron flux enhancement period presented peak values of ∼500 nT, which is concomitant with the Alfvénic fluctuations discussed above. Through these results, it is possible to confirm the occurrence of the substorms during these electron flux enhancements patterns observed in both case studies. According to Jaynes et al. (2015), substorms are a crucial element for the injection of low-energy (tens of keV) and medium-energy (30–300 keV) electrons in the inner magnetosphere, followed by the generation of the whistler-mode chorus waves and the high-energy electron flux enhancement. On the other hand, Da Silva et al. (2019) argue that during the global recovery in the outer radiation belt the conjunction of IMF Bz and IMF Alfvénic fluctuations alongside the presence of substorms play an important role in generating the ULF waves. Thereby, the low-energy and medium-energy electron flux enhancement, as well as both the whistler-mode chorus waves and ULF waves will be analyzed in the next section.

3.1.2. High-Energy Electron Flux Enhancements Versus the Chorus and ULF Waves

Whistler-mode chorus and ULF waves can play an important role in the electron acceleration in the outer radiation belt (Ma et al., 2016; Thorne, 2010; Thorne et al., 2013). The magnetic field spectrograms are presented to identify both the whistler-mode chorus and ULF wave activity during the Alfvénic fluctuation periods of case study 1 (Figure 5–top and second panels) and 2 (Figure 5–third and bottom panels). Figure 5 (top and third panels) show that chorus wave activity persists throughout the Alfvénic fluctuations time period, in conjunction with the injection of the low-energy (tens of keV) and medium-energy (30–300 keV) electron particles (Figures S36 and S37, respectively). This suggests that the Alfvénic fluctuations followed by the injection of the low-energy electron particles observed during the occurrence of the substorms may have been an important mechanism to generate these waves, as discussed by Jaynes et al. (2015).

Chorus waves typically occur in two distinct frequency bands: a lower-band (0.1 fce to 0.5 fce) and an upper-band (0.5 fce to fce), as shown in Figure 5 (top and third panels), where fce represents the equatorial

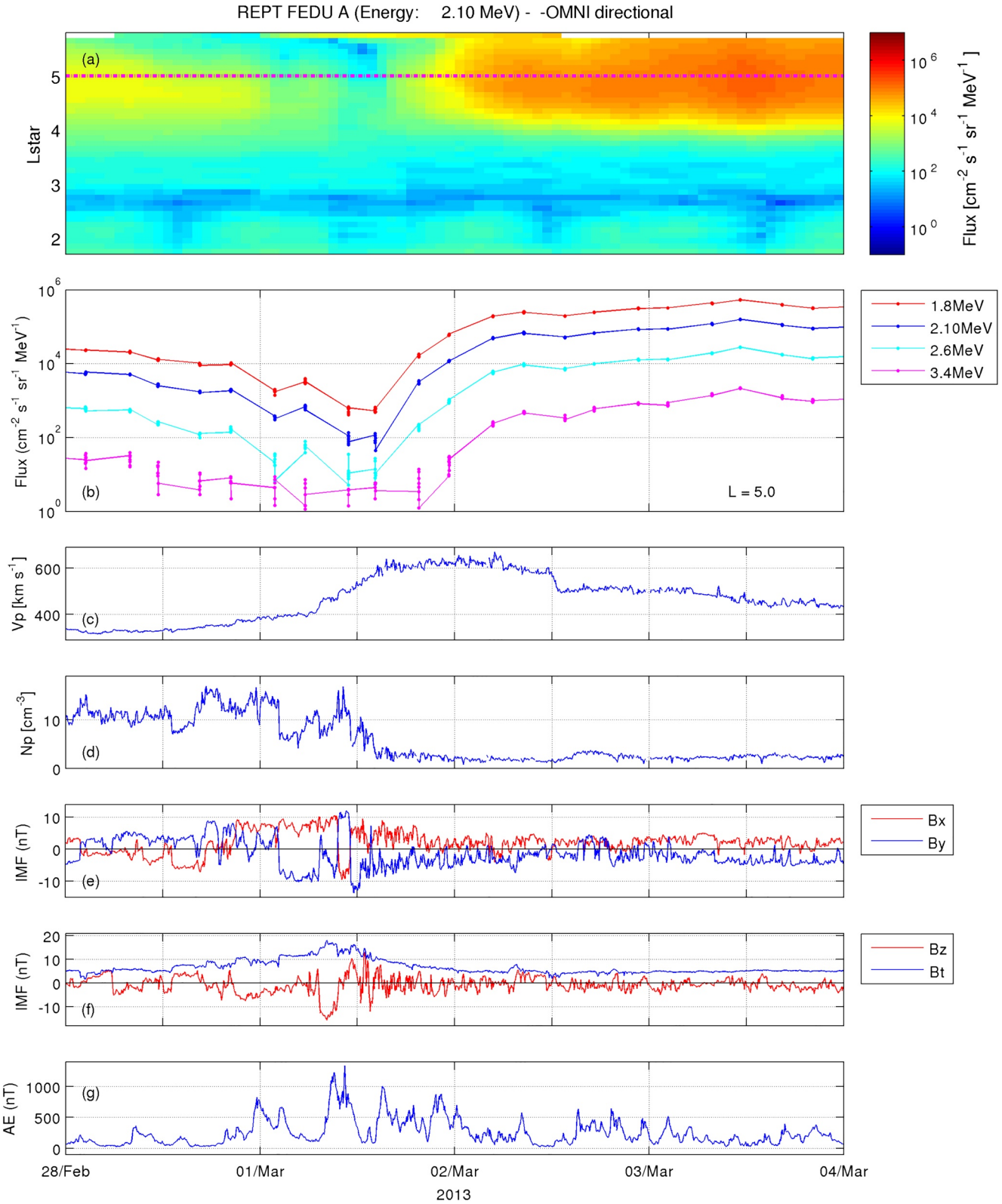
REPT FEDU A (Energy: 2.10 MeV) - -OMNI directional
(a)
Lstar
Flux [cm-2 s-1 sr-1 MeV-1]
(b)
L = 5.0
1.8MeV
2.10MeV
2.6MeV
3.4MeV
Vp [km s-1]
(c)
Np [cm-3]
(d)
IMF (nT)
(e)
Bx
By
(f)
Bz
Bt
AE (nT)
(g)
28/Feb
01/Mar
02/Mar
03/Mar
04/Mar
2013

Figure 3.

electron gyro-frequency (Koons & Roeder, 1990; Tsurutani & Smith, 1974). A visual inspection of the magnetic field spectrogram shows that the chorus waves in event 1 (Figure 5a–top panel) and event 2 (Figure 5b–third panel) occur in both the lower and upper-band. Upper-band chorus waves play a crucial role in the stochastic local acceleration of medium-energy electrons (<100 keV) up to relativistic levels in the outer radiation belt through energy diffusion (Ma et al., 2016; Shprits & Ni, 2009; Thorne et al., 2013; Xiao et al., 2010). This means that the high-energy electron enhancement pattern observed in both case studies may have been driven by these discussed mechanisms. In contrast, the chorus wave power in the lower-band can play a role in the local loss of relativistic electrons in the outer radiation belt through pitch angle scattering (Agapitov et al., 2015; Meredith et al., 2012). For this reason, only upper-band chorus wave power is relevant for the discussion of the events being analyzed here.

Figures 5a (second panel) and 5b (bottom panel) present evidence for strong ULF wave activity mainly in the first orbits, at the beginning of the high-energy electron flux enhancements observed in the outer radiation belt (Figures 1 and 2). The inward radial diffusion driven by ULF waves in drift resonance with trapped particles can allow energizing particle populations in the inner magnetosphere (e.g., Alves et al., 2017; Baker et al., 2005; Da Silva et al., 2019; Elkington et al., 2003; Hudson et al., 2000). Therefore, we can suggest inward radial diffusion as an essential dynamic mechanism responsible for the high energy electron flux enhancement observed in both events' outer radiation belt.

The chorus wave integrated power spectral density between 0.5 fce and fce (upper-band) during the Alfvénic fluctuation periods is presented in Figure 6 for each case study. The upper-band chorus wave activities are detected between $3.5 < L$-shell < 6.0 for both cases studies 1 and 2 through the Van Allen Probes A and B. These waves are observed intermittently and in different L-shells without a specific pattern for both case studies. Therefore, we suggest that the upper-band chorus waves may have contributed to the high-energy electron flux enhancements locally along the Alfvénic fluctuations periods intermittently in different L-shell.

A global vision of the ULF waves can be observed in Figure 7, which shows the ULF wave power calculated from the IMAGE network (ground-based data) for both the case studies 1 (panel a) and 2 (panel b). Strong ULF wave activity occurs preferentially at L-shells ≥ 4.0, except at 19:00 UT on March 1st (case study 1) and at 22:00UT on March 07th (case study 2).

ULF power analyzed as the ULF wave packets show an intermittent increase in both case studies. Case study 1 (panel a) indicates the first packet of the ULF wave activities from 12:00UT on March 1st and a strong signature starting at 17:00UT on March 1st, until 08:00UT on March 2nd. The second packet of ULF waves is recorded between 16:00UT on March 2nd and 06:00UT on March 3rd. Finally, the third packet of ULF waves is observed starting at 18:00UT on March 3rd.

Case study 2 (panel b) shows the first packet of the ULF wave activities from 09:00UT on March 7th, with the first strong signature at 12:00UT on March 7th, which persists until 12:00UT on March 8th. The second packet of the ULF waves occurs between 17:00UT on March 8th and 03:00UT on March 9th. The third packet of ULF waves started from 09:00UT on March 9th, persisting until 16:00UT on March 9th. Finally, the fourth packet is observed from 20:00UT on March 9th.

The intermittent ULF wave power observed in both case studies during the substorm activities suggest enhanced reconnection occurrences in the magnetotail (Angelopoulos et al., 2013; Sergeev et al., 2012). This dynamic can play an essential role in the generation and maintenance of the ULF and chorus waves, as discussed by Da Silva et al. (2019) and Jaynes et al. (2015), respectively. The maintenance of the ULF waves during the high-energy electron flux enhancements suggests that inward radial diffusion causes the enhancement pattern observed in both case studies. The main point here is the coincidence between the preferential L-shell ≥ 4.0 of the ULF wave activities and the high-energy electron flux enhancement pattern.

Figure 3. (a) Electron flux at 2.10 MeV energy as a function of L (vertical axis) and time (horizontal axis); (b) electron fluxes at 1.8 , 2.10 , 2.6, and 3.4 MeV energies at a fixed $L = 5.0$ location; (c) solar wind speed (Vp); (d) solar wind density (Np); (e) Bx component and By component of the Interplanetary Magnetic Field (IMF); (f) IMF intensity (Bt) and Bz component of the IMF. The electron fluxes are obtained by the relativistic Electron-Proton Telescope instrument onboard of the Van Allen Probe A. The Vp, Np, Bx, By, Bz and Bt are obtained by the Advanced Composition Explorer satellite in the Lagrangian L1 point. auroral electroject Indices are obtained at OMNIWeb: High Resolution OMNI (5-min averaged). Case study 1 occurred on February 28–March 03, 2013.

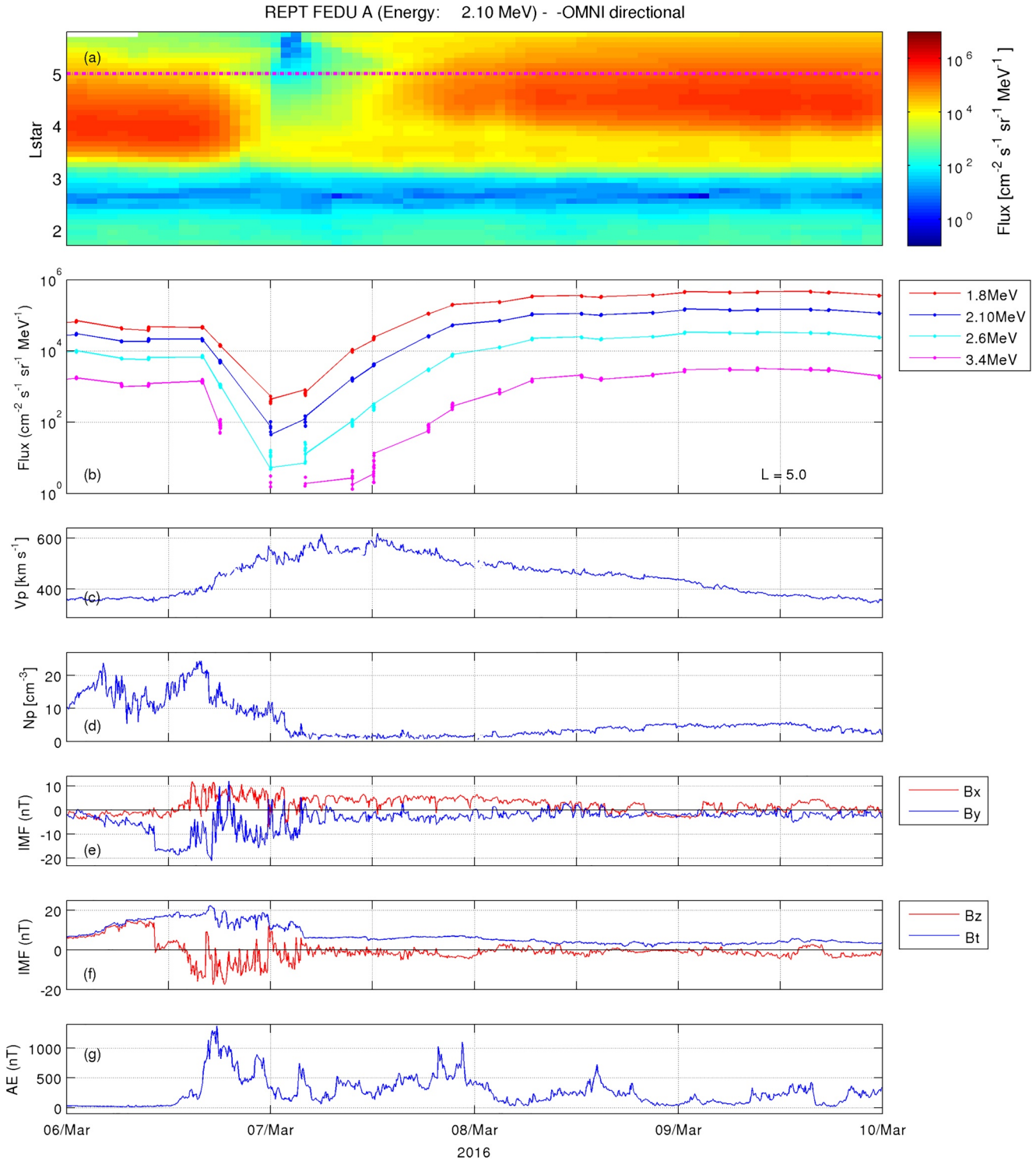

Figure 4. (a) Electron flux at 2.60 MeV energy as a function of *L* (vertical axis) and time (horizontal axis); (b) electron fluxes at 1.8, 2.10, 2.6 , and 3.4 MeV energies at a fixed $L = 5.0$ location; (c) solar wind speed (Vp); (d) solar wind density (Np); (e) Bx component and By component of the Interplanetary Magnetic Field (IMF); (f) IMF intensity (Bt) and Bz component of the IMF. The electron fluxes are obtained by the REPT instrument onboard of the Van Allen Probe A. The Vp, Np, Bx, By, Bz and Bt are obtained by the Advanced Composition Explorer satellite in the Lagrangian L1 point. auroral electroject Indices are obtained at OMNIWeb: High Resolution OMNI (5-min averaged). Case study 2 occurred on March 06–09, 2016.

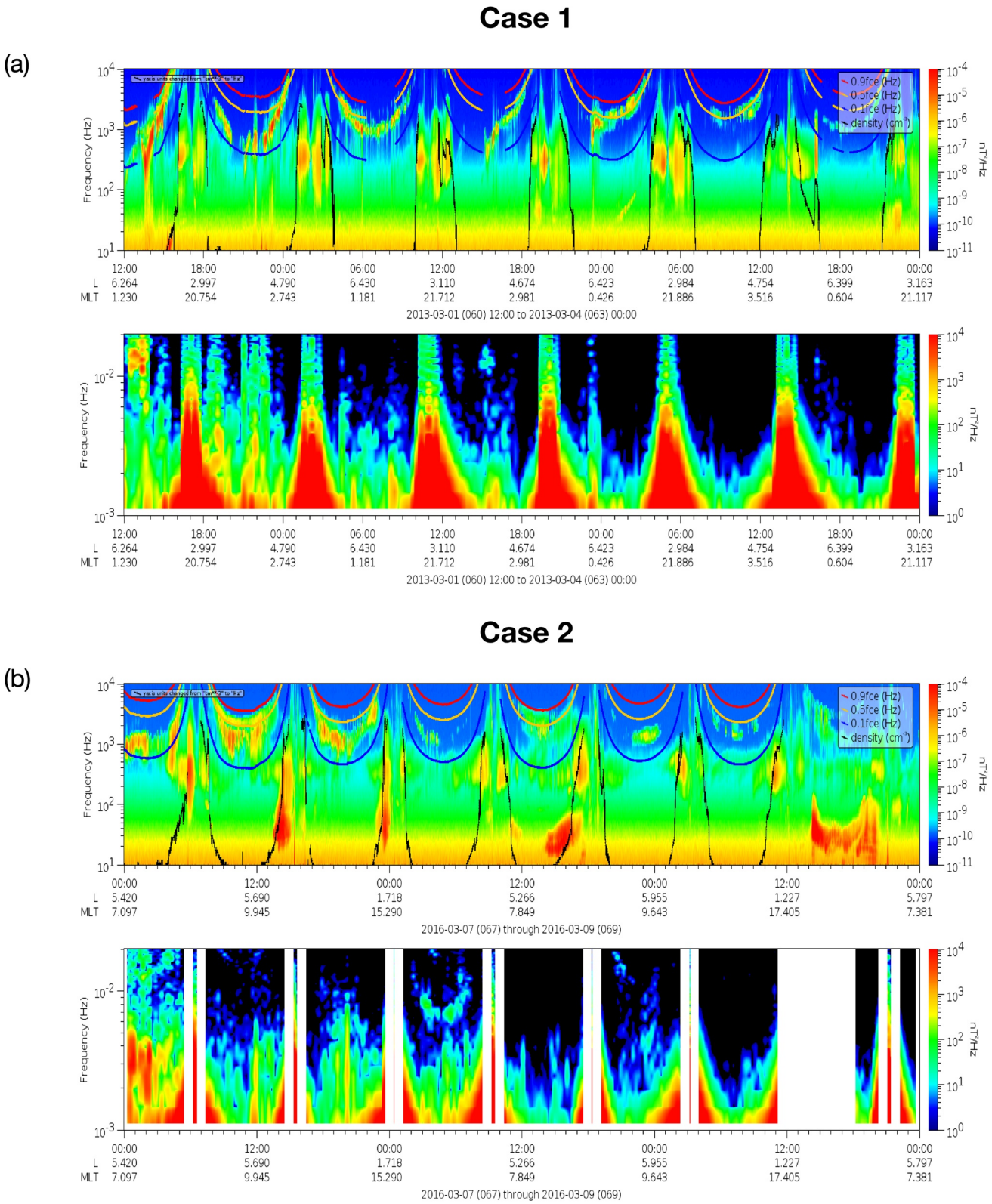
Case 1
(a)
0.9fce (Hz)
0.5fce (Hz)
0.1fce (Hz)
density (cm⁻³)
Frequency (Hz)
nT/√Hz
12:00 18:00 00:00 06:00 12:00 18:00 00:00 06:00 12:00 18:00 00:00
L 6.264 2.997 4.790 6.430 3.110 4.674 6.423 2.984 4.754 6.399 3.163
MLT 1.230 20.754 2.743 1.181 21.712 2.981 0.426 21.886 3.516 0.604 21.117
2013-03-01 (060) 12:00 to 2013-03-04 (063) 00:00
Case 2
(b)
00:00 12:00 00:00 12:00 00:00 12:00 00:00
L 5.420 5.690 1.718 5.266 5.955 1.227 5.797
MLT 7.097 9.945 15.290 7.849 9.643 17.405 7.381
2016-03-07 (067) through 2016-03-09 (069)

Figure 5.

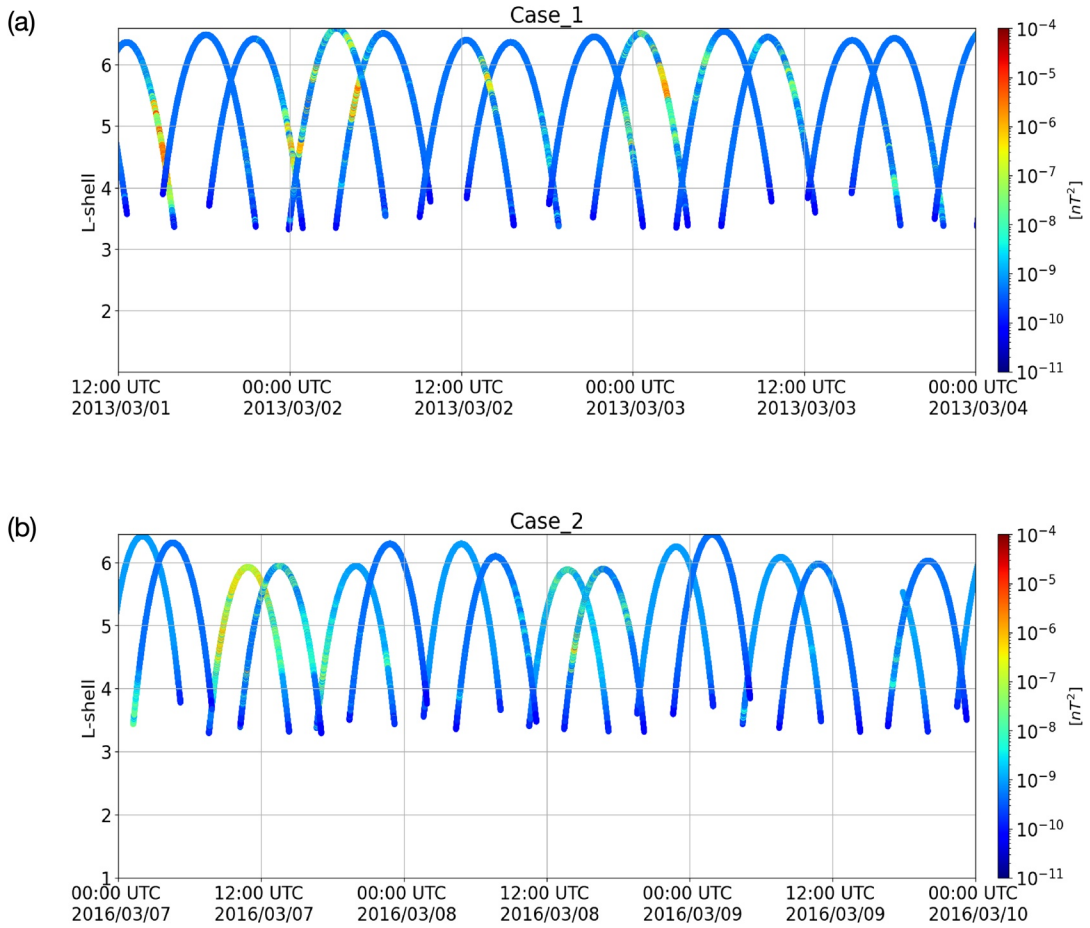

Figure 6. Chorus waves power spectral density detected between 0.5 fce and fce during the Alfvénic fluctuation periods. (Top panel) case 1 (12:00 UT March 1 to 00:00 UT March 04, 2013) and (bottom panel) case 2 (00:00 UT March 7 to 00:00 UT March 10, 2016). The magnetic field spectrograms and the equatorial electron gyro-frequency are obtained by the Electric and Magnetic Field Instrument Suite and Integrated Science instrument onboard of the Van Allen Probes A and B.

The ULF waves localization and the enhancement pattern are also analyzed statistically for 37 events in the next section.

3.2. Statistics of 37 Events

3.2.1. High-Energy Electron Flux Pattern Versus Interplanetary Medium Conditions

The dominant dynamic mechanisms responsible for the high-energy electron flux enhancement under the influences of the HSSs have been discussed individually in different case studies (Da Silva et al., 2019; Jaynes et al., 2015; Katsavrias et al., 2019; Souza et al., 2017), as well as statistically (e.g., Murphy et al., 2018; Turner et al., 2019). Although the physical processes have been widely discussed, the high-energy electron flux enhancement is still not well understood, mainly regarding the specific pattern studied here. Therefore, the interplanetary medium condition should be analyzed under the statistical point of view in order to identify the physical processes that drive this high-energy electron flux enhancement pattern. Addition-

Figure 5. EMFISIS' magnetic field spectrogram during the Alfvénic fluctuation periods, case 1 (12:00 UT March 1 to 00:00 UT March 04, 2013) and case 2 (00:00 UT March 7 to 00:00 UT March 10, 2016). (top and third panels) Chorus waves power spectral density. Red, orange, blue and black lines represent 0.9 fce, 0.5 fce, 0.1 fce and total electron density, respectively. (second and bottom panels) ultra-low frequency power spectral density. The magnetic field spectrograms, equatorial electron gyro-frequency and total electron density are obtained by the Electric and Magnetic Field Instrument Suite and Integrated Science instrument onboard of the Van Allen Probe A.

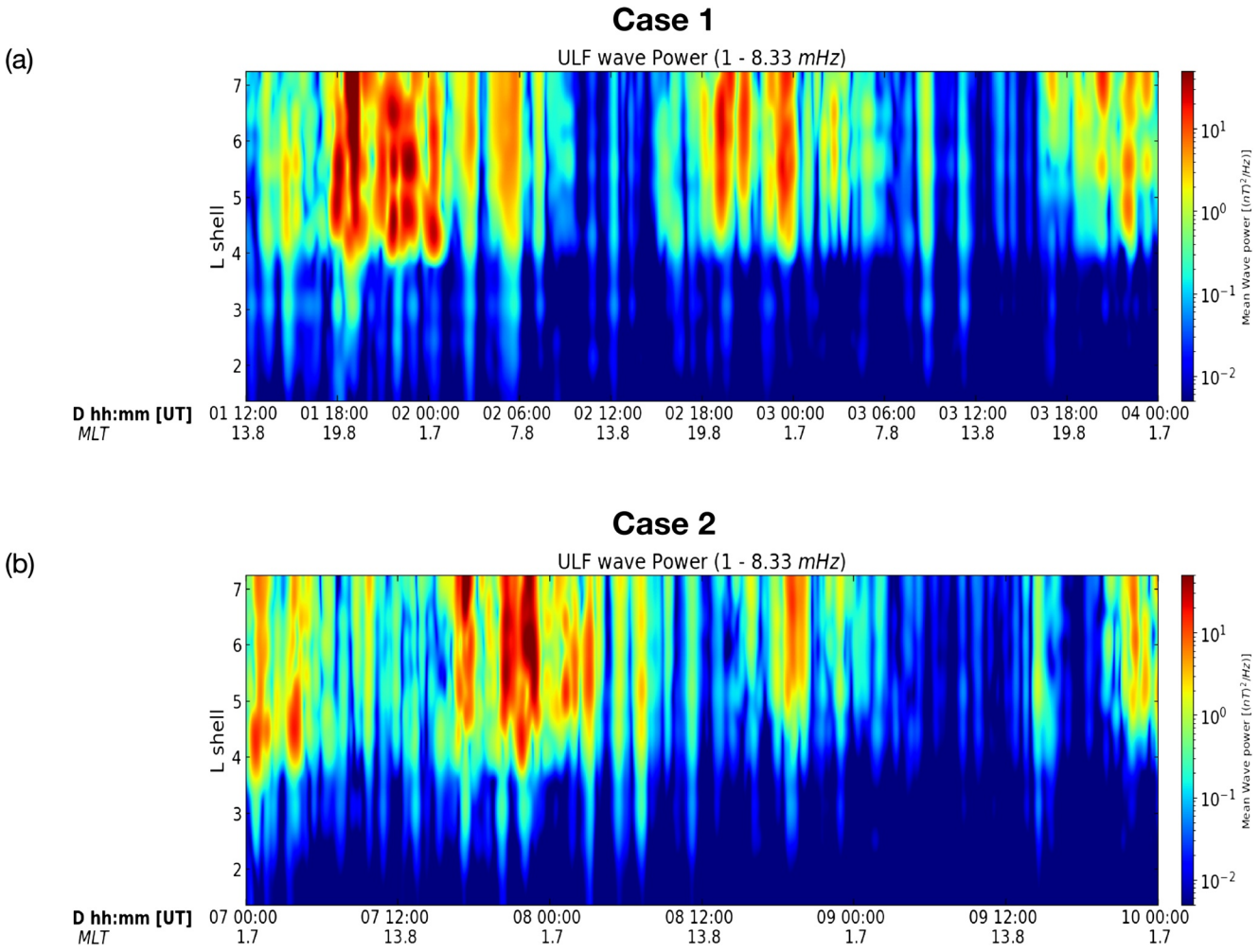

Figure 7. International Monitor for Auroral Geomagnetic Effects network's ultra-low frequency power spectral density in the 1–8.33 mHz frequency range (color's scale) as a function of *L*-shell and time during the Alfvénic fluctuation periods. (panel a) case study 1 (12:00 UT March 1 to 00:00 UT March 4, 2013). (panel b) case study 2 (00:00 UT March 7 to 00:00 UT 10 March, 2016).

ally, the ULF and chorus power spectral density and the linear correlation between the solar wind velocity components' variation versus the corresponding Alfvén velocity components are investigated and discussed individually for each of the 37 events (see Table A1–Appendix A).

High-energy electron flux enhancements pattern observed in 37 events during the Van Allen probes era are analyzed statistically through the Superposed Epoch analysis, as shown in Figure 8. The zero epoch was defined above. The solid blue line corresponds to the median, while the yellow lines are the upper and lower quartiles. Figure 8a presents the high-energy electron flux density (2.10 MeV) to $L = 5.0$, which shows that the electron flux enhancement increases by an order of magnitude in the first 20 h. After that, the electron flux enhancement increases approximately another order of magnitude in 40 h. This electron flux enhancement persists on average for 70 h in $L = 5.0$.

Figure 8b presents the high-energy electron flux density (2.10 MeV) at $L = 4.5$. During the first 20 h, the electron flux enhancement is insignificant (less than one order of magnitude). The electron flux enhancement at $L = 4.5$ reached one order of magnitude after 50 h in the upper quartile and 70 h in the lower quartile and the median. Figure 7c presents the high-energy electron flux density (2.10 MeV) at $L = 4.0$. No electron flux enhancement is observed in the upper or lower quartiles nor the median.

Figure 9 presents at Superposed Epoch analysis applied to the high-energy electron flux density at $L = 5.0$, solar wind parameters and the AE index, with the zero epoch as defined in the methodology above. The

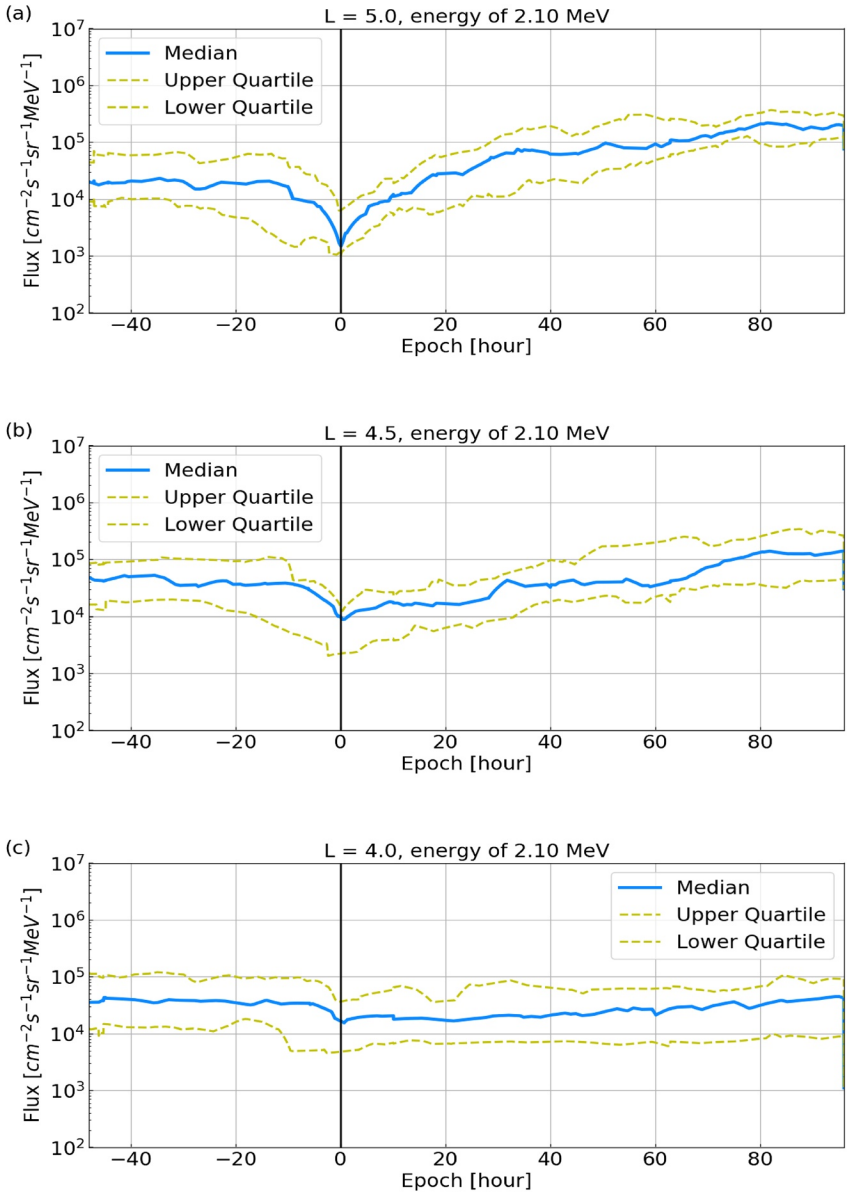

Figure 8. Superposed Epoch analysis of the high-energy electron flux ford 37 events. The solid blue line corresponds to the median, while the yellow dashed ones are the upper and lower quartiles. The high-energy electron flux density at 2.10 MeV energy is shown for *L*-shells at $L = 5.0$ (panel a), $L = 4.5$ (panel b) and $L = 4.0$ (panel c). The electron fluxes are obtained by the relativistic Electron-Proton Telescope instrument onboard of the Van Allen Probes.

high-energy electron flux density at $L = 5.0$ (panel a) increases two orders of magnitude at the first 20 h, while the solar wind speed (panel b) reaches ~450–470 km/s (lower quartiles), ~470–570 km/s (median), and ~570–620 km/s (upper quartiles). The solar wind proton density (panel c) decreases over the first 5 h (lower quartiles and median), remaining below the 5 cm^{-3} during the analyses.

The IMF components, Bx (panel d), By (panel e), and Bz (panel f), seem to oscillate consistently with Alfvénic fluctuations associated with the HSSs at the L1 Lagrangian point, with the Bz component oscillating around zero (median) preferentially negative and around −2 nT (lower quartiles). Close inspection is necessary to confirm the presence of the Alfvénic fluctuations during the high energy electron flux pattern. In order to do that, the linear correlation coefficient (CC) is calculated between the variations of the solar wind velocity components at the L1 location (ACE data) versus the corresponding Alfvén velocity components (Figures S1–S35). The CC is calculated for only 33 events because data are not available for events 23,

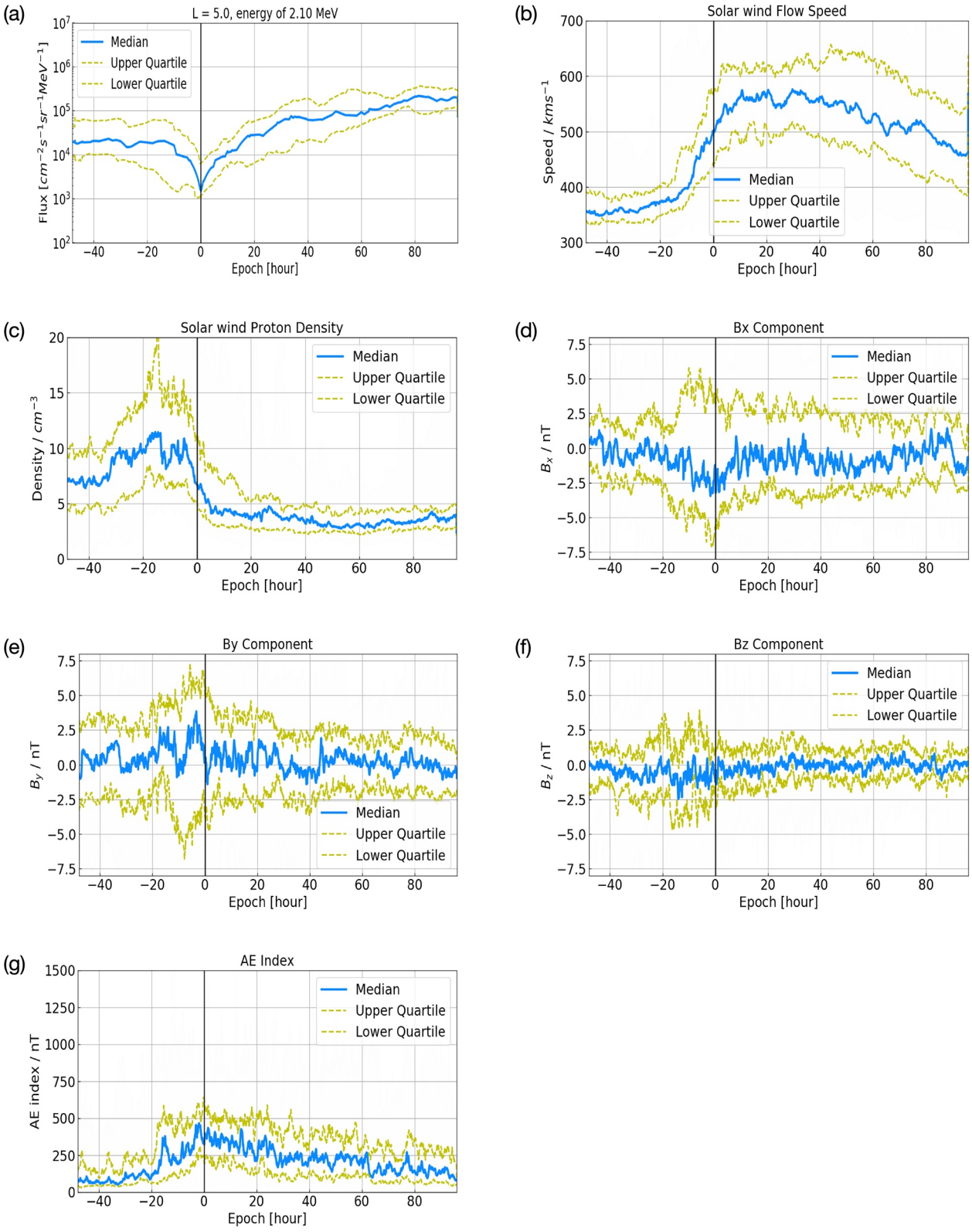
(a)
L = 5.0, energy of 2.10 MeV
Flux [$cm^{-2}s^{-1}sr^{-1}MeV^{-1}$]
Median
Upper Quartile
Lower Quartile
Epoch [hour]
(b)
Solar wind Flow Speed
Speed / kms^{-1}
Median
Upper Quartile
Lower Quartile
Epoch [hour]
(c)
Solar wind Proton Density
Density / cm^{-3}
Median
Upper Quartile
Lower Quartile
Epoch [hour]
(d)
Bx Component
B_x / nT
Median
Upper Quartile
Lower Quartile
Epoch [hour]
(e)
By Component
B_y / nT
Median
Upper Quartile
Lower Quartile
Epoch [hour]
(f)
Bz Component
B_z / nT
Median
Upper Quartile
Lower Quartile
Epoch [hour]
(g)
AE Index
AE index / nT
Median
Upper Quartile
Lower Quartile
Epoch [hour]

Figure 9.

26, 31, and 36, as seen in Table A1. The results confirm that the CC for the X, Y, and Z components of the solar wind velocity exceeds 0.6 for 31 events and reaches ∼0.9 for several events. Only for events 25 and 29, the CC attained higher values in only two of the three components, as shown in Figures S24–25 and S28–29. It means that 100% of the solar wind events analyzed here are Alfvénic in nature. This kind of oscillations may provide prolonged intervals of southward Bz (Gonzalez et al., 1994), initiate reconnection on the Earth's dayside magnetopause, and, consequently, drive moderate-intensity geomagnetic storms (Tsurutani et al., 1995) and recurrent substorms.

High resolution (5-min averaged) AE index (panel g) indicates peaks next to 400 nT (median) and 750 nT (upper quartiles) after the zero epoch, which suggests the presence of the substorms during the global recovery of the high-energy electron flux. Alfvénic fluctuations associated with the HSSs, Bz southward, and substorms can contribute to the occurrences of the low-energy electron particle injections in the outer radiation belt and to the generation of magnetospheric waves in a wide range of frequency (Da Silva et al., 2019; James et al., 2013, 2016; Jauer et al., 2019; Jaynes et al., 2015; Souza et al., 2017; Thorne et al., 2013; Yeoman et al., 2010).

3.2.2. High-Energy Electron Flux Pattern Versus the Chorus and ULF Waves

Wave-particle resonant interactions can accelerate electron particles to high-energy levels in the inner magnetosphere. Local acceleration mechanism driven by whistler-mode chorus and radial diffusion ULF waves may have played an essential role in the high-energy electron flux enhancement pattern under the influence of the HSSs. Therefore, investigating chorus and ULF wave activity during the high-energy electron flux enhancement is crucial to understanding the main physical processes that drove this enhancement pattern.

The generation of the chorus and ULF waves in these 37 events, occurred under the influence of the Alfvénic fluctuations is considerably high, once the Chorus (ULF) wave activity was observed in 89.2% (100%) of the events. The role of each wave in this electron flux enhancement pattern is essential. Thereby, the local acceleration driven by chorus waves and inward radial diffusion driven by ULF waves are discussed here through Superposed Epoch Analysis applied to the ULF and chorus waves.

Figure 10 present the Superposed Epoch Analysis applied to the chorus magnetic field wave power integrated in the 0.5 fce - fce frequency band at $L = 5.5$ (panel a), $L = 5.0$ (panel b), $L = 4.5$ (panel c), $L = 4.0$ (panel d), $L = 3.5$ (panel e) and $L = 3.0$ (panel f), respectively. The solid blue line corresponds to the median value, while the yellow dashed lines are the upper and lower quartiles. We analyze the median values and upper quartile. The solid blue lines and yellow dashed lines at $L = 3.0$ (panel f) present few measurements and are considerably lower, which means lower chorus wave power at the slot region. Thus, the analyses will be concentrated inside the outer radiation belt, that is, in the $3.5 \leq L \leq 5.5$ interval. The chorus power (solid blue lines) shows a gradual increase in L (panel a–e) without differences before and after the zero epoch. The upper quartile also shows a gradual increase in L, and additionally it, shows a considerable chorus wave power increase around the zero epoch at $L = 5.5$, $L = 5.0$, $L = 4.5$, $L = 4.0$ (panels a–d). It means that the HSSs contributed to the increase of the integrated chorus wave power during the decrease in the electron flux. Furthermore, the integrated chorus power does not present a significant response during the influence of the Alfvénic fluctuations, except after 60 h. Therefore, we suggest that the chorus waves contributed locally through local acceleration to these high-energy electron flux enhancements (see Ozeke et al., 2020).

The ULF wave power ($>\log_{10}$ (1) nT^2/Hz–IMAGE data) results observed for each event (Table A1–Appendix A) suggest that the specific electron flux enhancement pattern beginning at $L > 4.0$ can be associated with the ULF wave activity's depth in this radiation belt. The ULF waves activity has been concentrated (on average) from L-shell ≥ 4.0 in 100%, L-shell ≥ 4.3 in 45%, and L-shell ≥ 4.5 in 33% of the 33 events (with data).

Figure 9. Superposed Epoch analysis of the high-energy electron flux at $L = 5.0$, solar wind parameters and auroral electroject (AE) index to 37 events. The solid blue line corresponds to the median, while the yellow ones are the upper and lower quartiles. The high-energy electron flux density (2.10 MeV) at $L = 5.0$ (panel a), solar wind speed (Vp) (panel b); solar wind density (Np) (panel c); Bx component of the IMF (panel d), By component of the interplanetary magnetic field (IMF) (panel e); Bz component of the IMF (panel f) and AE Index (panel g). The electron fluxes are obtained by the relativistic Electron-Proton Telescope instrument onboard of the Van Allen Probes. The Vp, Np, Bx, By and Bz are obtained by the Advanced Composition Explorer satellite in the Lagrangian L1 point. AE Index is obtained at OMNIWeb: High Resolution OMNI (5-min averaged).

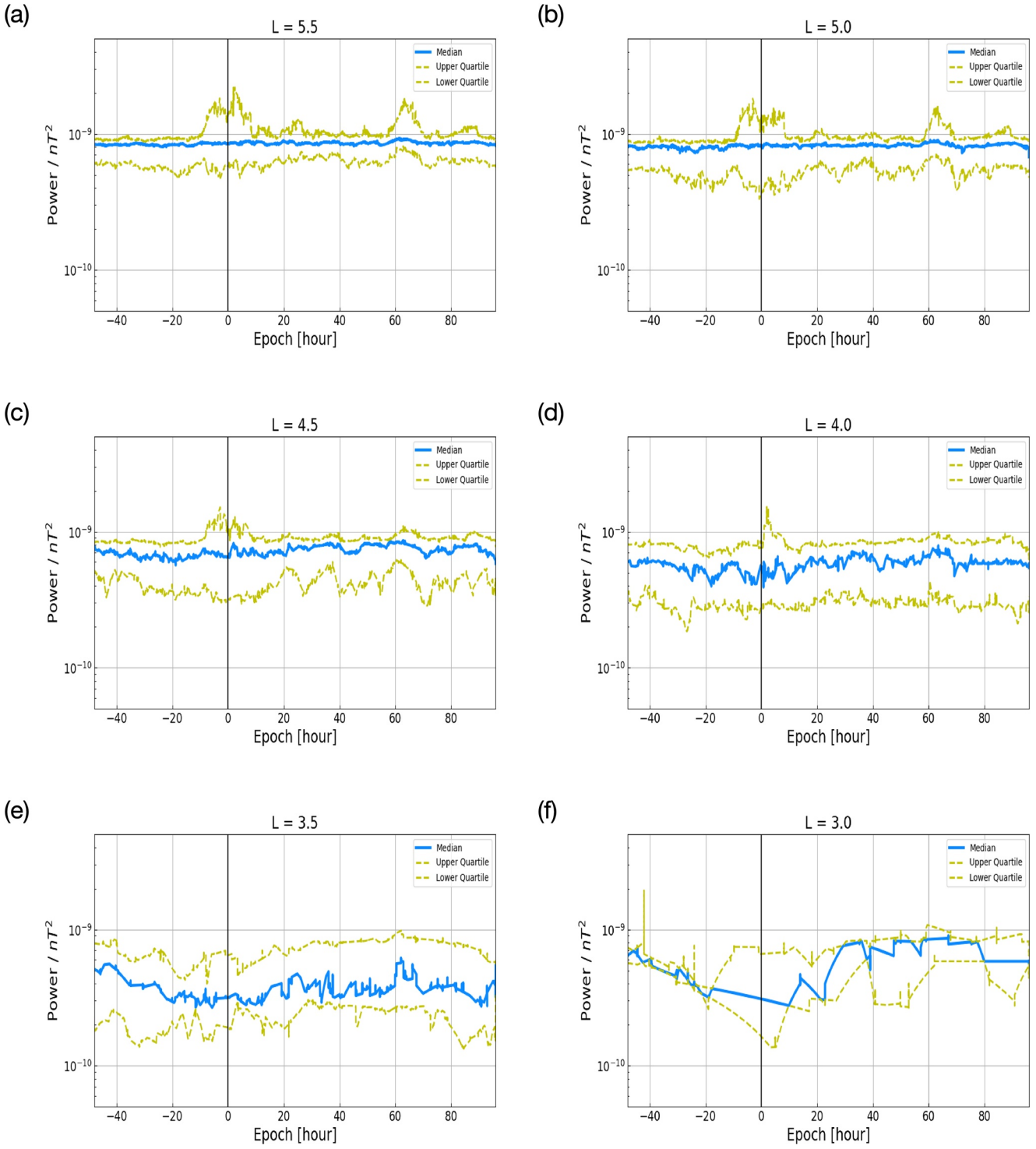

Figure 10. Superposed Epoch Analysis of the Chorus waves (0.5 fce - fce) Power Spectral integrated at *L*-shell = 5.5 (panel a); 5.0 (panel b); 4.5 (panel c); 4.0 (panel d); 3.5 (panel e); 3.0 (panel f). The solid blue line corresponds to the median value, while the yellow ones are the upper and lower quartiles. The magnetic field spectrograms and the equatorial electron gyro-frequency are obtained by the Electric and Magnetic Field Instrument Suite and Integrated Science instrument onboard of the Van Allen Probes A.

It means that during this electron flux enhancement pattern, the ULF wave activity localized in L may have played a crucial role in the enhancements. However, before showing the Superposed Epoch Analysis applied to the ULF waves, it is necessary to present the main parameters used to estimate the radial diffusion driven by these waves, as such the ULF wave polarization modes (see Da Silva et al., 2019).

The ULF wave modes are characterized as fast (compressional), poloidal and toroidal according to the predominant PSD component, that is, parallel magnetic field ($B_{||}$), azimuthal electric field (E_φ), and radial electric field (E_r), respectively. The inward radial diffusion driven by ULF waves can energize seed electrons to relativistic energies through drift resonant interactions. The efficiency of the ULF polarization modes has been widely studied (see e.g., Da Silva et al., 2019; Elkington, 2006; Perry et al., 2005; Ukhorskiy et al., 2009). Elkington et al. (2003) and Ukhorskiy et al. (2005) showed that the poloidal polarization mode is a more efficient accelerator than the toroidal mode. Therefore, the condition for the azimuthal particle drift motion resonant interact with the poloidal wave electric field is $\omega = m\omega d$, where ω is the wave frequency, m is the azimuthal wavenumber and ω_d is the particle drift frequency.

The distribution function of particles undergoing stochastic motion in L shell should satisfy the radial diffusion equation (Schulz & Lanzerotti, 1974). In Equation 1, f is the phase space density of electrons, in which the first and second adiabatic invariants are conserved, D_{LL} is the radial diffusion coefficient and τ is the electron lifetime.

$$\frac{\partial f}{\partial t} = L^2 \frac{\partial}{\partial L}\left[\frac{D_{LL}}{L^2}\frac{\partial f}{\partial L}\right] - \frac{f}{\tau}. \tag{1}$$

The analytic form of the D_{LL} may be derived from the Hamiltonian formulation (Brizard & Chan, 2001; Fei et al., 2006). D_{LL} (Equation 2) is the sum of the diffusion coefficient due to uncorrelated azimuthal electric field (Equation 3) and the compressional magnetic field (Equation 4) perturbations, D_{LL}^E and D_{LL}^B, respectively.

$$D_{LL} = D_{LL}^E + D_{LL}^B, \tag{2}$$

$$D_{LL}^E = \frac{1}{8B_E^2 R_E^2} L^6 \sum_m P_m^E\left(m\omega_d\right), \text{and} \tag{3}$$

$$D_{LL}^B = \frac{M^2}{8q^2\gamma^2 B^2 R_E^4} L^4 \sum_m m^2 P_m^B\left(m\omega_d\right). \tag{4}$$

where the M is the first adiabatic invariant, γ is the relativistic correction factor, B_E is the equatorial magnetic field strength at the surface of the Earth, R_E is the Earth's radius and q is the electron charge. The terms $P_m^E\left(m\omega_d\right)$ and $P_m^B\left(m\omega_d\right)$ represent the power spectral density of the electric and magnetic perturbations with azimuthal wave number, at the wave frequency, which satisfy the drift resonance condition.

The components of the electric and magnetic field were derived from the EFW electric field data and EMFISIS magnetic field data, respectively, in which we applied a Butterworth bandpass filter. Since the E_x component is not provided in the L2 EFW, the third component of electric field was estimated assuming that E.B = 0. The error associated with this method grows as the angle between the background magnetic field and the spin plane are close to zero. The criteria for reduce this error was to exclude the data when this angle is smaller than ~6° (Ali et al., 2016). To identify the polarization modes of the ULF waves we rotate the electric and magnetic field vectors to the field-aligned coordinate system as follows: consider a location s = (x, y, z) in space where there is a local magnetic field vector B, the parallel (||) direction is represented by b = B/|B|, the azimuthal (ϕ) direction is given by the cross product between b and the unitary position vector s/|s|, and the radial (r) direction completes the orthonormal system being positive radially outwards (see Da Silva et al., 2019).

Figures 11 and 12 present the Superposed Epoch Analysis applied to the ULF wave power integrated of the azimuthal component of the electric field (P_m^E) and the parallel component of the magnetic field (P_m^B) at

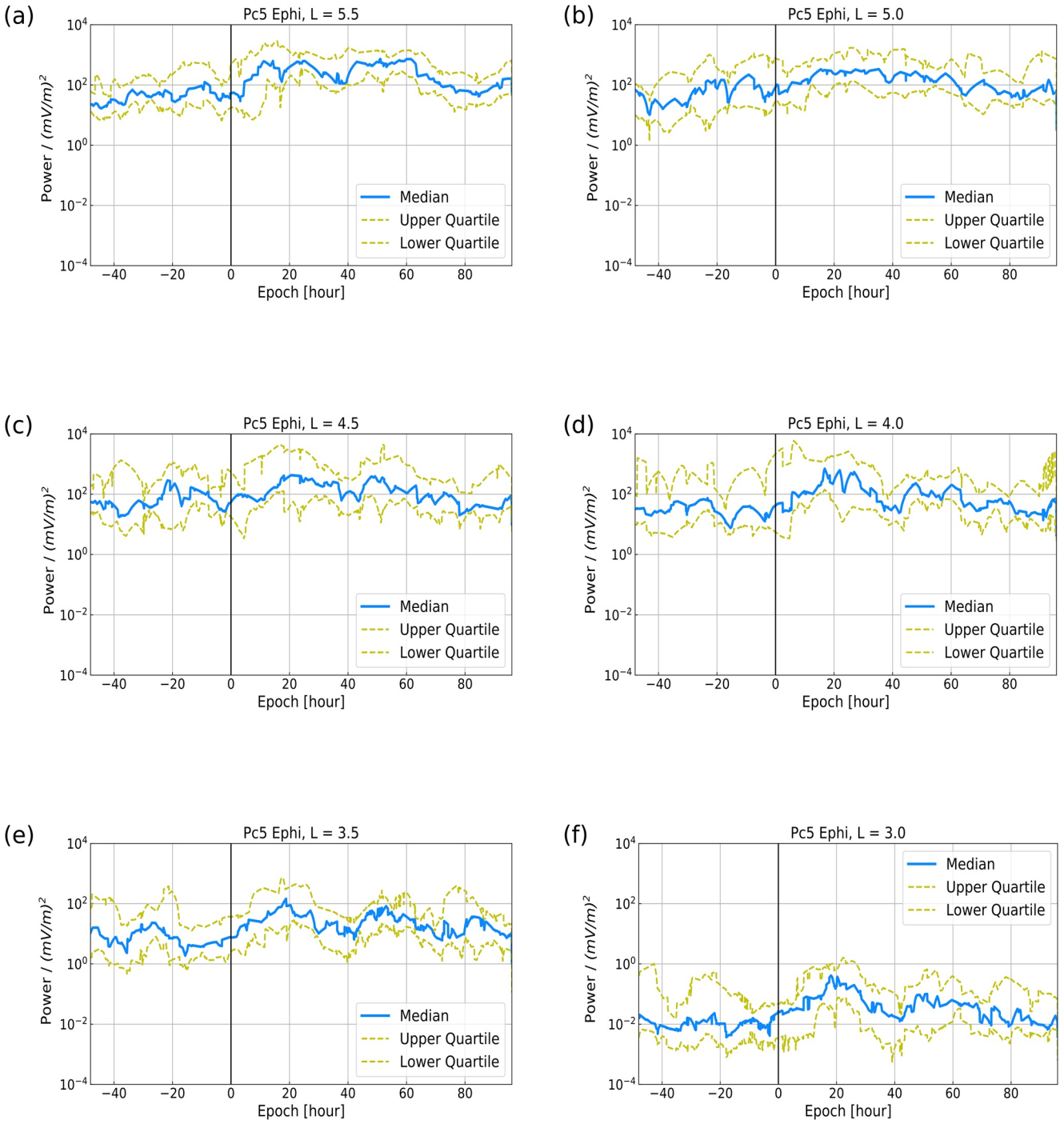

Figure 11. Superposed Epoch Analysis of the ultra-low frequency (ULF) waves Power Spectral integrated for the azimutal component of the electric field recorded at L-shell = 5.5 (panel a); 5.0 (panel b); 4.5 (panel c); 4.0 (panel d); 3.5 (panel e); 3.0 (panel f). The solid blue line corresponds to the median value, while the yellow ones are the upper and lower quartiles. The ULF power was performed for the electric field from Electric Field and Waves instrument onboard Van Allen Probes A.

$L = 5.5$ (panel a), $L = 5.0$ (panel b), $L = 4.5$ (panel c), $L = 4.0$ (panel d), $L = 3.5$ (panel e) and $L = 3.0$ (panel f), respectively. The solid blue line corresponds to the median value, while the yellow ones are the upper and lower quartiles. We analyze the median values of both P_m^E and P_m^B along the L and the time. This analysis can provide insight into the sources of the wave power, as well as the key physical drivers of the radial diffusion coefficients (Sandhu et al., 2021).

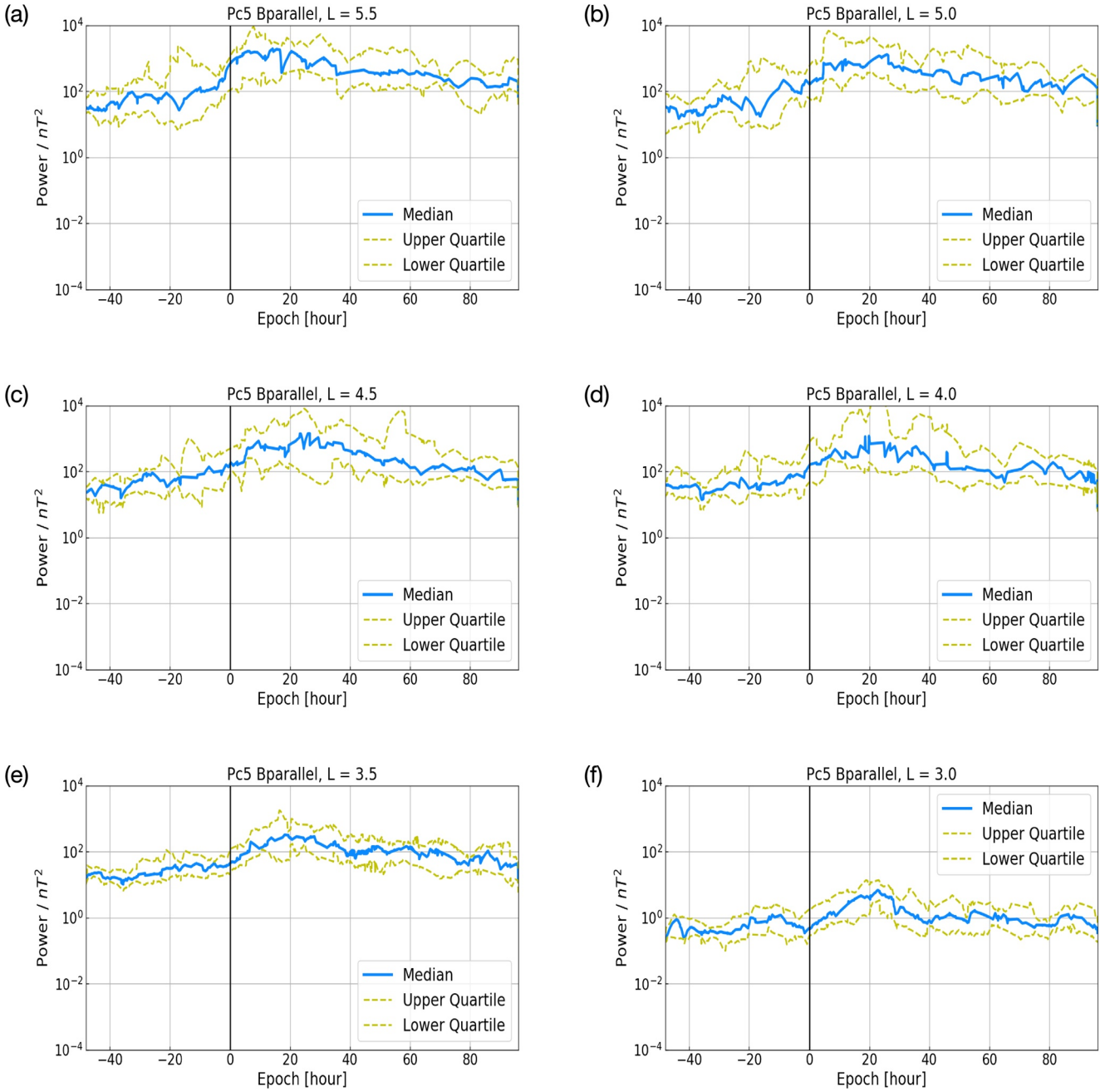

Figure 12. Superposed Epoch Analysis of the ultra-low frequency (ULF) waves Power Spectral integrated for the parallel component of the magnetic field recorded at *L*-shell = 5.5 (panel a); 5.0 (panel b); 4.5 (panel c); 4.0 (panel d); 3.5 (panel e); 3.0 (panel f). The solid blue line corresponds to the median value, while the yellow ones are the upper and lower quartiles. The ULF power was performed for the magnetic field from Electric and Magnetic Field Instrument Suite and Integrated Science instrument onboard Van Allen Probes A.

The integrated ULF power of the azimuthal component of the electric field (Figure 11) shows the solid blue line at $L = 3.0$ (panel f) considerably low, which means low P_m^E at the slot region. Before the zero epoch within the outer radiation belt, especially for $4.0 \leq L \leq 5.5$, the P_m^E shows the median around 10^1 $(\text{mV/m})^2$ and 10^2 $(\text{mV/m})^2$, with few incursions above 10^2 $(\text{mV/m})^2$ at $L = 5.5$ (panel a), 5.0 (panel b), and 4.5 (panel c). While the P_m^E after the zero epoch within the outer radiation belt ($3.5 \leq L \leq 5.5$) shows a considerable increase. For $L = 3.5$, we observe that P_m^E fluctuates around 10^1 $(\text{mV/m})^2$ with only one incursion above 10^2 $(\text{mV/m})^2$ during ~19 h. For $L = 4.0$, the P_m^E presents values around 10^2 $(\text{mV/m})^2$, presenting below

10^2 nT^2 the most of the time analyzed. For $L = 4.5$, P_m^E is concentrated around 10^2 $(mV/m)^2$ with few incursions below that. For $L = 5.0$, P_m^E is presented values around 10^2 $(mV/m)^2$, showing above 10^2 $(mV/m)^2$ the most of the time analyzed. For $L = 5.5$, P_m^E fluctuates next 10^3 $(mV/m)^2$ with few incursions below that. Thus, we can suggest that the P_m^E increased (median values) under the influences of the Alfvénic fluctuations, presenting a gradient after the zero epoch related to the L.

Figure 12 shows integrated ULF power of the parallel component of the magnetic field. The solid blue line at $L = 3.0$ (panel f) shows values that remained below 10^0 nT^2 during most of the time, which means low P_m^B at the slot region. Before the zero epoch within the outer radiation belt ($3.5 \leq L \leq 5.5$), the P_m^B shows median values around 10^1 and 10^2 nT^2, with few incursions above 10^2 nT^2 at $L = 5.5$ (panel a), 5.0 (panel b), 4.5 (panel c), and 4 (panel d). While the P_m^B after the zero epoch within the outer radiation belt ($3.5 \leq L \leq 5.5$) shows a considerable increase in each L, which is clear a gradient related to the L, as such observed in P_m^E and discussed above. Therefore, P_m^B (compressional mode) and P_m^E (poloidal mode) increased (median values) under the influence of the Alfvénic fluctuations.

The values assumed for these terms, P_m^E and P_m^B, in each L are crucial to calculate the inward radial diffusion driven by ULF waves (Equation 2) in each L, as well is important to calculate the phase space density of electrons (f) (Equation 1) in each L. Therefore, a gradual increase of these terms, P_m^E and P_m^B, in L implies a gradual increase of the high-energy electron flux in L, as observed in Figure 7. Thereby, we can suggest that the ULF wave activity localized in L is decisive to the position of the high-energy electron flux enhancement pattern ($L > 4$).

3.3. Schematic of the Ideal Setup and Sequence for High-Energy Electron Flux Enhancements Pattern

A schematic of the ideal setup and sequence for strong enhancement of outer belt electrons >1 MeV was proposed by Jaynes et al. (2015). Here, we propose an adaptation to this scheme, including new key ingredients, as ULF waves and Alfvénic fluctuations, and considering the 37 events. Thereby, Figure 13 presents a further schematic of the ideal setup and sequence for high-energy electron flux enhancements pattern. The key ingredients are:

1. Alfvénic fluctuations at L1 Lagrangian point (new)
2. Bz component preferentially southward
3. Magnetospheric substorms
4. Low-to medium-energy electron particle injections in the inner magnetosphere
5. Generation of the chorus waves
6. Local acceleration driven by chorus waves
7. Generation of the ULF waves (new)
8. Radial diffusion driven by ULF waves (new)

The first key ingredient is the Alfvénic fluctuations, which, for all events, are associated with the HSSs. Bz component is preferentially southward, but it is essential to highlight that the Bz southward is not necessarily strong, only on averaged southward value is needed (Da Silva et al., 2019 and Souza et al., 2017), the second key ingredient. This IMF conditions load substantial energy into the Earth's magnetotail. In turn, this can lead to a magnetospheric substorm onset (McPherron et al., 1973), the third key ingredient. This substorm generally is accompanied by an injection of low-energy (tens of keV) and medium-energy (30–300 keV) electrons into the Earth's inner magnetosphere. Low-energy and medium-energy electrons are named respectively, source populations and seed populations of particles (e.g., Baker et al., 1996; Jaynes et al., 2015 and references therein). The seed population is the fourth key ingredient. The source population of electrons can feed free energy into electromagnetic waves in the lower chorus band through their anisotropic angular distributions (Thorne et al., 2013), the fifth key ingredient. The chorus waves can interact resonantly with the seed electron population to promote local acceleration, the sixth key ingredient. The injection of low-energy and medium-energy electrons into the Earth's inner magnetosphere during the substorms can also drive the generation of ULF waves (see James et al., 2013, 2016; Yeoman et al., 2010), the seventh ingredient. The ULF waves can also interact resonantly with the seed electron population to

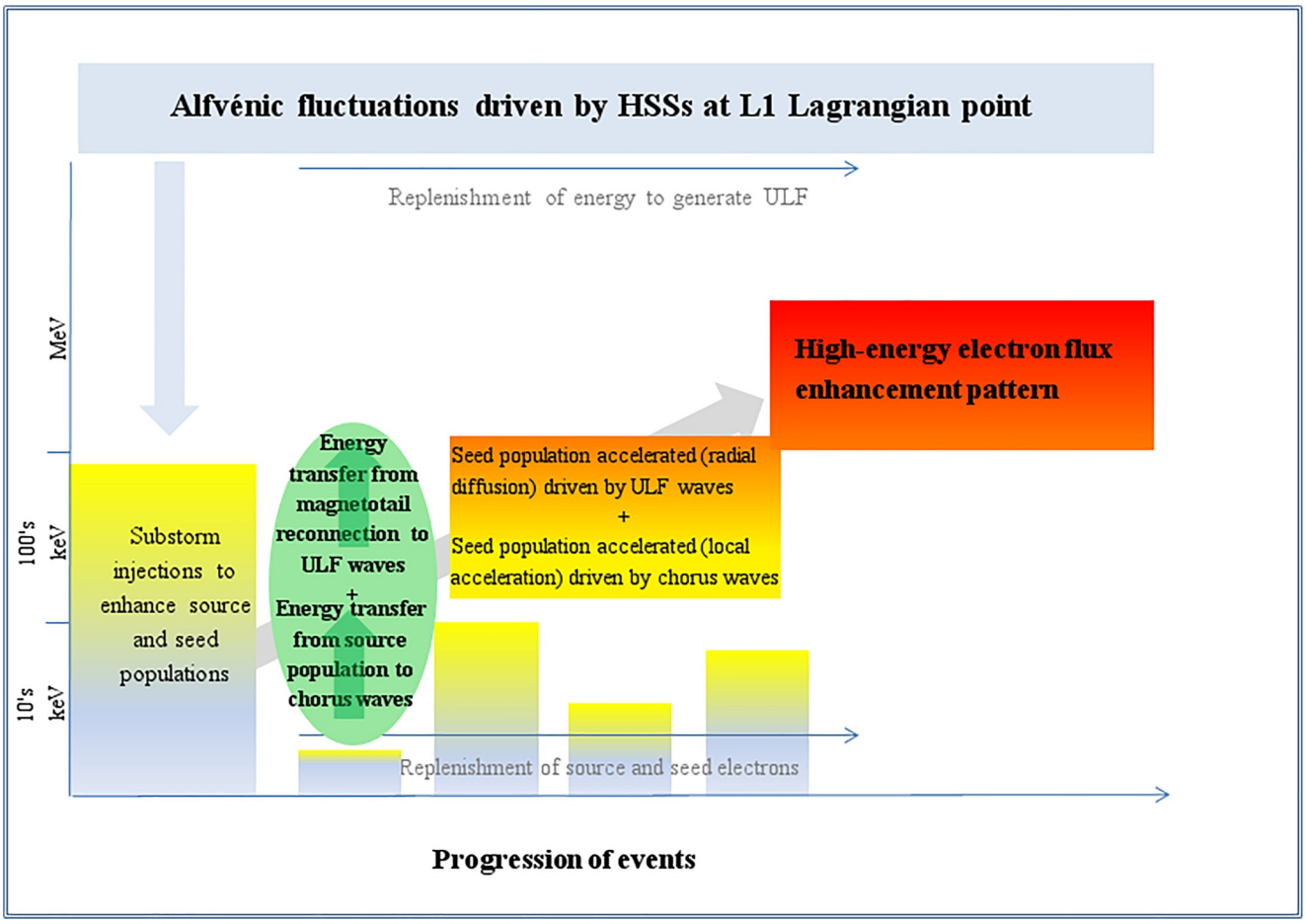

Figure 13. Schematic of the ideal setup and sequence for high-energy electron flux enhancements pattern. Adapted from Jaynes et al. (2015).

accelerate the particles through the radial diffusion mechanism (Da Silva et al., 2019 and Souza et al., 2017), as shown in the eighth key ingredient.

4. Conclusions

In this paper we determined the key ingredients responsible for the high-energy electron flux enhancement in the outer radiation belt that occur under the influence of the high speed solar wind streams, considering the importance of the new key ingredients and the intensity of some others. The first new key ingredient is the Alfvénic fluctuations at the L1 Lagrangian point. They are essential because all the high-energy electron flux enhancement coincided with them. The Alfvénic fluctuations' period is also concomitant with both the magnetospheric substorms, generally moderate, and the Bz component to the southward, on average. These ingredients trigger the low-to medium-energy electron particle injections in the inner magnetosphere, consequently generating the chorus and ULF waves. After that, the medium-energy electron particles injected in the outer radiation belt interact with the chorus and ULF waves triggering the local acceleration and inward radial diffusion, respectively, followed by the high-energy electron flux enhancement in the outer radiation belt.

The upper-band chorus power did not present a significant change (variation) after the zero epoch, except after 60 h. Therefore, we suggest that the chorus waves contributed locally through the local acceleration to the high-energy electron flux enhancement pattern. Otherside, the ULF power (P_m^E and P_m^B) presented a gradual radially increase after zero epoch. It means the ULF wave activity localized in L is a decisive

ingredient to trigger the physical processes responsible for the high-energy electron flux enhancement pattern ($L > 4$).

The importance of this result refers to the new key ingredients that can be considered in the particle models for improvement of the high-energy electron flux variability predictions. We will develop the future works considering these new key ingredients in a neural network model to predict the high-energy electron flux variability and quantify the importance of the new ingredients inside the particle model.

Appendix A: List of Events

Table A1 presents the number of each event (first column); the time when the HSSs were measured at L1 Lagrangian point (second column); the chorus wave's starts time during the enhancements (third column); the ULF wave's L-shell minimum during enhancement (fourth column); and the coefficient correlation (CC) between the variation of the solar wind velocity components at L1 location versus the corresponding Alfvén velocity > 0.6, considering Vx, Vy, and Vz (fifth column).

Table A1
List of Events

Number	HSS date and time at L1 Lagrangian point	Chorus waves' start time during enhancement	ULF waves' Lshell minimum during enhancement	Alfvén velocity (C.C. > 0.6) VxVyVz
1	2013-02-28 15:00	y/from 18UT–01/Mar	y/Lshell ~ 4.5	y
2	2014-01-01 14:00	y/from 12UT–02/Jan	y/Lshell ~ no data	y
3	2014-02-09 11:27	y/from 11UT–09/Feb	y/Lshell ~ 4.5	y
4	2014-09-19 00:00	y/from 19UT–21/Sep	y/Lshell ~ 4.5	y
5	2014-12-06 12:05	y/from 11UT–07/Dec	y/Lshell ~ 4.5	y
6	2015-02-17 12:13	y/from 18UT–18/Feb	y/Lshell ~ 4.5	y
7	2015-04-15 03:15	y/from 21UT–15/Apr	y/Lshell ~ 4.2	y
8	2015-05-12 17:20	y/from 13UT–13/May	y/Lshell ~ 4.2	y
9	2015-06-08 00:16	Not chorus wave activity	y/Lshell ~ 4.5	y
10	2015-07-10 18:30	Not chorus wave activity	y/Lshell ~ 4.0	y
11	2015-08-06 06:24	Not chorus wave activity	y/Lshell ~ 4.2	y
12	2015-10-04 01:00	y/from 22UT–04/Oct	y/Lshell ~ 4.2	y
13	2015-11-03 05:29	y/from 21UT–03/Nov	y/Lshell ~ 4.3	y
14	2016-03-06 09:00	y/from 08UT–07/Mar	y/Lshell ~ 4.0	y
15	2016-07-07 00:00	y/from 10UT–08/Jul	y/Lshell ~ 4.2	y
16	2016-08-22 10:00	y/from 10UT–24/Aug	y/Lshell ~ 4.3	y
17	2016-09-26 07:05	y/from 15UT–26/Sep	y/Lshell ~ 4.5	y
18	2016-11-10 16:38	y/from 12UT–11/Nov	y/Lshell ~ 4.5	y
19	2016-11-24 05:14	y/from 13UT–24/Nov	y/Lshell ~ 4.2	y
20	2016-12-07 18:40	y/from 11UT–08/Dec	y/Lshell ~ 4.5	y
21	2016-12-21 03:37	y/from 20UT–21/Dec	y/Lshell ~ 4.2	y
22	2017-01-03 07:00	y/from 08UT–05/Jan	y/Lshell ~ 4.2	y
23	2017-01-26 07:11	y/from 12UT–27/Jan	y/Lshell ~ 4.1	No data
24	2017-03-21 00:00	Not chorus wave activity	y/Lshell ~ 4.1	y
25	2017-07-08 23:13	y/from 04UT–10/Jul	y/Lshell ~ 4.3	y to Vx,Vz and y to Vx,Vy
26	2017-08-04 07:00	y/from 05UT–04/Aug	y/Lshell ~ 4.2	No data
27	2017-08-17 08:00	y/from 20UT–17/Aug	y/Lshell ~ 4.2	y
28	2017-10-10 16:50	y/from 01UT–12/Oct	y/Lshell No data	y

Table A1
Continued

Number	HSS date and time at L1 Lagrangian point	Chorus waves' start time during enhancement	ULF waves' Lshell minimum during enhancement	Alfvén velocity (C.C. > 0.6) VxVyVz
29	2017-12-04 15:00	y/from 15UT–05/Dec	y/Lshell ~ 4.7	y to Vx,Vz and y to Vy,Vz
30	2017-12-16 21:00	y/from 19UT–17/Dec	y/Lshell ~ 4.1	Y
31	2018-01-21 06:00	y/from 21UT–21/Jan	y/Lshell ~ 4.5	No data
32	2018-02-16 10:30	y/from 08UT–17/Feb	y/Lshell ~ 4.2	y
33	2018-03-14 12:00	y/from 02UT–15/Mar	y/Lshell ~ 4.0	y
34	2018-04-09 06:00	y/from 05UT–10/Apr	y/Lshell ~ 4.3	y
35	2018-05-31 14:11	y/from 10UT–01/Jun	y/Lshell ~ 4.1	y
36	2018-07-23 23:00	y/from 21UT–24/Jul	y/Lshell No data	No data
37	2018-08-14 21:48	y/from 17UT–15/Aug	y/Lshell No data	y

(Left to right) Event Number; date and time when the HSSs were measured at L1 Lagrangian point (DONKI repository); Chorus wave activity start time during the enhancements pattern (Van Allen Probes data); ULF waves' *L*-shell minimum during enhancement (IMAGE data); and the coefficient correlation (CC) between the variation of the solar wind velocity components at L1 location versus the corresponding Alfvén velocity > 0.6, considering Vx, Vy, and Vz (see Figures S1–S35).

Abbreviations: coefficient correlation, CC; Database of Notifications, Knowledge, Information, DONKI; high-speed solar wind streams, HSS; International Monitor for Auroral Geomagnetic Effects, IMAGE; ultra-low frequency, ULF.

Acknowledgments
We acknowledge the NASA Van Allen Probes, Harlan E. Spence (PI ECT; University of New Hampshire), John Wygant (PI EFW; University of Minnesota) and Craig Kletzing (PI EMFISIS; University of Iowa) for use of data. We acknowledge the NASA ACE satellite, Edward Stone (PI ACE; Caltech). We also acknowledge the IMAGE network, Kirsti Kauristie (PI IMAGE, Finnish Meteorological Institute). The authors acknowledge the SuperMAG PI Dr. Jesper W. Gjerloev the whole SuperMAG team for data availability and the website convenience for IMAGE data download. Ligia Alves da Silva and Paulo Jauer are grateful for financial support from China-Brazil Joint Laboratory for Space Weather. This research was also supported by the National Natural Science Foundation of China (Nos. 42074201 and 41674145). M. V. Alves thanks CNPq/MCTIC (310900/2016-6). Luis Eduardo Vieira thanks CNPq/MCTIC (Grants 307404/2016-1), TED-004/2020-AEB and PO-20VB.0009. L. R. Alves thanks to CNPq/MCTIC (301476/2018-7). Souza acknowledges support from the Brazilian National Council for Scientific and Technological Development (CNPq) PCI Grant 300982/2020-8. Work at NASA/GSFC was supported by the Van Allen Probes mission. Marchezi J. P. thanks to CNPq/MCTI (140962/2017-4) and China-Brazil Joint Laboratory for Space Weather. O. A. was supported by NASA grants 80NNSC19K0848, 80NSSC19K0264, 80NSSC20K0218, and NSF grant 1914670.

Data Availability Statement

All the data used are available at: ECT: https://cdaweb.gsfc.nasa.gov/pub/data/rbsp/. EFW: http://themis.ssl.berkeley.edu/data/rbsp/efwcmds/. EMFISIS: https://emfisis.physics.uiowa.edu/Flight/. ACE: http://www.srl.caltech.edu/ACE/ASC/DATA/browse-data/. IMAGE: http://supermag.jhuapl.edu/mag/. AE index: https://omniweb.gsfc.nasa.gov/form/omni_min.html. DONKI: https://kauai.ccmc.gsfc.nasa.gov/DONKI/search/.

References

Agapitov, O. V., Artemyev, A. V., Mourenas, D., Mozer, F. S., & Krasnoselskikh, V. (2015). Empirical model of lower band chorus wave distribution in the outer radiation belt. *Journal of Geophysical Research: Space Physics*, *120*, 10425–10442. https://doi.org/10.1002/2015JA021829

Ali, A. F., Malaspina, D. M., Elkington, S. R., Jaynes, A. N., Chan, A. A., Wygant, J., & Kletzing, C. A. (2016). Electric and magnetic radial diffusion coefficients using the Van Allen probes data. *Journal of Geophysical Research: Space Physics*, *121*, 9586–9607. https://doi.org/10.1002/2016JA023002

Alves, L. R., Da Silva, L. A., Souza, V. M., Sibeck, D. G., Jauer, P. R., Vieira, L. E. A., et al. (2017). Outer radiation belt dropout dynamics following the arrival of two interplanetary coronal mass ejections. *Geophysical Research Letters*, *43*, 978–987. https://doi.org/10.1002/2015GL067066

Angelopoulos, V., Runov, A., Zhou, X.-Z., Turner, D. L., Kiehas, S. A., Li, S. S., & Shinohara, I. (2013). Electromagnetic energy conversion at reconnection fronts. *Science*, *341*(6153), 1478–1482. https://doi.org/10.1126/science.1236992

Baker, A. B., Li, X., & Selesnick, R. S. (2005). Modeling the radiation belt electrons with radial diffusion driven by the solar wind. *Space Weather*, *3*, S10003. https://doi.org/10.1029/2004SW000118

Baker, D. N., Blake, J. B., Klebesadel, R. W., & Higbie, P. R. (1986). Highly relativistic electrons in the Earth's outer magnetosphere: Lifetimes and temporal history 1979–1984. *Journal of Geophysical Research*, *91*(A4), 4265–4276. https://doi.org/10.1029/JA091iA04p04265

Baker, D. N., Hoxie, V. C., Batiste, S., Bolton, M., Li, X., Elkington, S. R., et al. (2013). The Relativistic Electron-Proton Telescope (REPT) Instrument on Board the Radiation Belt Storm Probes (RBSP) Spacecraft: Characterization of Earth's radiation belt high-energy particle populations. *Space Science Reviews*, *179*(1–4), 337–381. https://doi.org/10.1007/s11214-012-9950-9

Baker, D. N., Pulkkinen, T. I., Angelopoulos, V., Baumjohann, W., & McPherron, R. L. (1996). The neutral line model of substorms: Past results and present view. *Journal of Geophysical Research*, *101*(A6), 12975–13010. https://doi.org/10.1029/95JA03753

Blake, J. B., Carranza, P. A., Claudepierre, S. G., Clemmons, J. H., Crain, W. R., Jr., & Dotan, Y. (2013). The magnetic electron ion spectrometer (MagEIS) instruments aboard the radiation belt storm probes (RBSP) spacecraft. *Space Science Reviews*, *179*, 383–421. https://doi.org/10.1007/s11214-013-9991-8

Brizard, A. J., & Chan, A. A. (2001). Relativistic bounce-averaged quasilinear diffusion equation for low-frequency electromagnetic fluctuations. *Physics of Plasmas*, *8*(11), 4762–4771. https://doi.org/10.1063/1.1408623

Burlaga, L. F., & Lepping, R. P. (1977). The causes of recurrent geomagnetic storms. *Planetary and Space Science*, *25*, 1151–1160. https://doi.org/10.1016/0032-0633(77)90090-3

Cameron, T., & Jackel, B. (2016). Quantitative evaluation of solar wind time-shifting methods. *Space Weather*, *14*(11), 973–981. https://doi.org/10.1002/2016SW001451

Chen, Y., Reeves, G. D., Friedel, R. H. W., & Cunningham, G. S. (2014). Globaltime-dependent chorus maps from low-Earth-orbit electron precipitation and Van Allen Probes data. *Geophysical Research Letters*, *41*, 755–761. https://doi.org/10.1002/2013GL05918

Claudepierre, S. G., Elkington, S. R., & Wiltberger, M. (2008). Solar wind driving of magnetospheric ULF waves: Pulsations driven by velocity shear at the magnetopause. *Journal of Geophysical Research*, *113*, A05218. https://doi.org/10.1029/2007JA012890

Da Silva, L. A., Sibeck, D., Alves, L. R., Souza, V. M., Jauer, P. R., Claudepierre, S. G., et al. (2019). Contribution of ULF wave activity to the global recovery of the outer radiation belt during the passage of a high-speed solar wind stream observed in September 2014. *Journal of Geophysical Research: Space Physics*, *124*, 1660–1678. https://doi.org/10.1029/2018JA026184

Echer, E., Gonzalez, W. D., Tsurutani, B. T., & Gonzalez, A. L. C. (2008). Interplanetary conditions causing intense geomagnetic storms (Dst ≤−100 nT) during solar cycle 23 (1996–2006). *Journal of Geophysical Research*, *113*, A05221. https://doi.org/10.1029/2007JA012744

Elkington, S. R. (2006). A review of ULF interactions with radiation belt electrons, in Magnetospheric ULF Waves: Synthesis and New Directions. In T. Kazue, P. J. Chi, and R. E. Denton, (Eds.) *Geophys. Monogr. Ser*., vol. 169, pp. 177–194. AGU.

Elkington, S. R., Hudson, M. K., & Chan, A. A. (1999). Acceleration of relativistic electrons via drift-resonant interaction with toroidal-mode Pc-5 ULF oscillations. *Geophysical Research Letters*, *26*(21), 3273–3276, https://doi.org/10.1029/1999GL003659

Elkington, S. R., Hudson, M. K., & Chan, A. A. (2003). Resonant acceleration and diffusion of outer zone electrons in an asymmetric geomagnetic field. *Journal of Geophysical Research*, *108*, 1116. https://doi.org/10.1029/2001JA009202

Fei, Y, Chan, A. A., Elkington, S. R., & Wiltberger, M. J. (2006). Radial diffusion and MHD particle simulations of relativistic electron transport by ULF waves in the September 1998 storm. *Journal of Geophysical Research*, *111*, A12209. https://doi.org/10.1029/2005JA011211

Forsyth, C., Rae, I. J., Murphy, K. R., Freeman, M. P., Huang, C.-L., Spence, H. E., et al. (2016). What effect do substorms have on the content of the radiation belts? *Journal of Geophysical Research - A: Space Physics*, *121*(7), 6292–6306. https://doi.org/10.1002/2016JA022620

Funsten, H. O., Skoug, R. M., Guthrie, A. A., MacDonald, E. A., Baldonado, J. R., Harper, R. W., et al. (2013). Helium, Oxygen, Proton, and Electron (HOPE) mass spectrometer for the radiation belt storm probes mission. *Space Science Reviews*, *179*, 423–484. https://doi.org/10.1007/s11214-013-9968-7

Gonzalez, W. D., Joselyn, J., Kamide, Y., Kroehl, H., Rostoker, G., Tsurutani, B., & Vasyliunas, V. (1994). What is a geomagnetic storm? *Journal of Geophysical Research*, *99*(A4), 5771–5792. https://doi.org/10.1029/93ja02867

Gonzalez, W. D., Tsurutani, B. T., & Clua-Gonzalez, A. L. (1999). Interplanetary origin of geomagnetic storms. *Space Science Reviews*, *88*, 529–562. https://doi.org/10.1023/A:1005160129098

Gurnett, D. A., & O'Brien, B. J. (1964). High-latitude geophysical studies with satellite Injun 3: 5. Very-low-frequency electromagnetic radiation. *Journal of Geophysical Research*, *69*(1), 65–89. https://doi.org/10.1029/JZ069i001p00065

Hartley, D. P., Denton, M. H., Green, J. C., Onsager, T. G., Rodriguez, J. V., & Singer, H. J. (2013). Case studies of the impact of high-speed solar wind streams on the electron radiation belt at geosynchronous orbit: Flux, magnetic field, and phase space density. *Journal of Geophysical Research: Space Physics*, *118*, 6964–6979. https://doi.org/10.1002/2013JA018923

Hudson, M. K., Elkington, S. R., Lyon, J. G., & Goodrich, C. C. (2000). Increase in relativistic electron flux in the inner magnetosphere: ULF wave mode structure. *Advances in Space Research*, *25*, 2327–2337. https://doi.org/10.1016/S0273-1177(99)00518-9

James, M. K., Yeoman, T. K., Mager, P. N., & Klimushkin, D. Y. (2013). The spatio-temporal characteristics of ULF waves driven by substorm injected particles. *Journal of Geophysical Research: Space Physics*, *118*, 1737–1749. https://doi.org/10.1002/jgra.50131

James, M. K., Yeoman, T. K., Mager, P. N., & Klimushkin, D. Y. (2016). Multi radar observations of substorm-driven ULF waves. *Journal of Geophysical Research: Space Physics*, *121*, 5213–5232. https://doi.org/10.1002/2015JA022102

Jamison, B., & Regal, R. (1979). The statistical significance of data from superposed epoch analyses. Solar-Terrestrial Influences of Weather and Climate. In Billy M., McCormac, Thomas A. Seliga (Eds.), *Proceedings of a Symposium/Workshop held at the Fawcett Center for Tomorrow*, *The Ohio State University, Columbus, Ohio, 24–28 August, 1978*. (Vol. 13, pp. 175–179). Springer. (ISBN: 978-94-009-9428-7). https://doi.org/10.1007/978-94-009-9428-7_17

Jauer, P. R., Wang, C., Souza, V. M., Alves, M. V., Alves, L. R., Pádua, M. B., et al. (2019). A global magneto hydrodynamic simulation study of ultra-low-frequency wave activity in the inner magnetosphere: Corotating interaction region + Alfvénic fluctuations. *The Astrophysical Journal*, *886*, 59. https://doi.org/10.3847/1538-4357/ab4db5

Jaynes, A. N., Ali, A. F., Elkington, S. R., Malaspina, D. M., Baker, D. N., Li, X., et al. (2018). Fast diffusion of ultra-relativistic electrons in the outer radiation belt: 17 March 2015 storm event. *Geophysical Research Letters*, *45*, 10874–10882. https://doi.org/10.1029/2018GL079786

Jaynes, A. N., Baker, D. N., Singer, H. J., Rodriguez, J. V., Loto'aniu, T. M., Ali, A. F., et al. (2015). Source and seed populations for relativistic electrons: Their roles in radiation belt changes. *Journal of Geophysical Research: Space Physics*, *120*, 7240–7254. https://doi.org/10.1002/2015JA021234

Kalliokoski, M. M. H., Kilpua, E. K. J., Osmane, A., Turner, D. L. A. N. J., Turc, L., George, H., et al. (2020). Outer radiation belt and inner magnetospheric response to sheath regions of coronal mass ejections: A statistical analysis. *Ann. Geophys.*, *38*, 683–701. https://doi.org/10.5194/angeo-38-683-2020

Katsavrias, C., Sandberg, I., Li, W., Podladchikova, O., Daglis, I. A., Papadimitriou, C., et al. (2019). Highly relativistic electron flux enhancement during the weak geomagnetic storm of April–May 2017. *Journal of Geophysical Research: Space Physics*, *124*, 4402–4413. https://doi.org/10.1029/2019JA026743

Kavosi, S., & Raeder, J. (2015). Ubiquity of Kelvin-Helmholtz waves at Earth's magnetopause. *Nature Communications*, *6*, 7019. https://doi.org/10.1038/ncomms8019

Kilpua, E. K. J., Hietala, H., Koskinen, H. E. J., Fontaine, D., & Turc, L. (2013). Magnetic field and dynamic pressure ULF fluctuations in coronal-mass-ejection-driven sheath regions. *Annales Geophysicae*, *31*, 1559–1567. https://doi.org/10.5194/angeo-31-1559-2013

Kilpua, E. K. J., Hietala, H., Turner, D. L., Koskinen, H. E. J., Pulkkinen, T. I., Rodriguez, J. V., et al. (2015). Unraveling the drivers of the storm time radiation belt response. *Geophysical Research Letters*, *42*, 3076–3084. https://doi.org/10.1002/2015GL063542

Kivelson, M. G., & Southwood, D. J. (1985). Resonant ULF waves: A new interpretation. *Geophysical Research Letters*, *12*, 49–52. https://doi.org/10.1029/GL012I001P00049

Kletzing, C. A., Kurth, W. S., Acuna, M., MacDowall, R. J., Torbert, R. B., Averkamp, T., et al. (2013). The Electric and Magnetic Field Instrument Suite and Integrated Science (EMFISIS) on RBSP. *Space Science Reviews*, *179*(1–4), 127–181. https://doi.org/10.1007/s11214-013-9993-6

Koons, H. C., & Roeder, J. L. (1990). A survey of equatorial magnetospheric wave activity between 5 and 8 RE. *Planetary and Space Science*, *38*(10), 1335–1341. https://doi.org/10.1016/0032-0633(90)90136-E

Lyons, L. R., Kim, H.-J., Xing, X., Zou, S., Lee, D.-Y., Heinselman, C., et al. (2009). Evidence that solar wind fluctuations substantially affect global convection and substorm occurrence. *Journal of Geophysical Research*, *114*, A11306. https://doi.org/10.1029/2009JA014281

Ma, Q., Mourenas, D., Artemyev, A., Li, W., Thorne, R. M., & Bortnik, J. (2016). Strong enhancement of 10–100 keV electron fluxes by combined effects of chorus waves and time domain structures. *Geophysical Research Letters*, *43*, 4683–4690. https://doi.org/10.1002/2016GL069125

Mann, I. R., Wright, A. N., Mills, K. J., & Nakariakov, V. M. (1999). Excitation of magnetospheric waveguide modes by magnetosheath flows. *Journal of Geophysical Research*, *104*(A1), 333–353. https://doi.org/10.1029/1998JA900026

Marchezi, J. P. (2020). Evaluation of ULF activity on the electron transportation in the outer radiation belt IBI: 8JMKD3MGP-3W34R/42GSLS8. (sid.inpe.br/mtc-m21c/2020/05.20.19.22-TDI). *Tese (Doutorado em Geofisica Espacial/Ciências do Ambiente Solar-Terrestre) - Instituto Nacional de Pesquisas Espaciais (INPE), São José dos Campos*, 2020. (p. 139). Retrieved from http://urlib.net/rep/8JMKD3MGP3W34R/42GSLS8

Mauk, B. H., Fox, N. J., Kanekal, S. G., Kessel, R. L., Sibeck, D. G., & Ukhorskiy, A. (2012). Science objectives and rationale for the radiation belt storm probes mission. *Space Science Reviews*, *179*, 3–27. https://doi.org/10.1007/s11214-012-9908-y

McPherron, R. L., Russell, C. T., & Aubry, M. P. (1973). Satellite studies of magnetospheric substorms on August 15, 1968, 9, phenomenological model for substorms. *Journal of Geophysical Research*, *78*, 3131–3149. https://doi.org/10.1029/JA078i016p03131

Meredith, N. P., Horne, R. B., Sicard-Piet, A., Boscher, D., Yearby, K. H., Li, W., & Thorne, R. M. (2012). Global model of lower band and upper band chorus from multiple satellite observations. *Journal of Geophysical Research*, *117*, A10225. https://doi.org/10.1029/2012JA017978

Miyoshi, Y., & Kataoka, R. (2005). Ring current ions and radiation belt electrons during geomagnetic storms driven by coronal mass ejections and corotating interaction regions. *Geophysical Research Letters*, *32*, L21105. https://doi.org/10.1029/2005GL024590

Miyoshi, Y., Kataoka, R., Kasahara, Y., Kumamoto, A., Nagai, T., & Thomsen, M. F. (2013). High-speed solar wind with southward interplanetary magnetic field causes relativistic electron flux enhancement of the outer radiation belt via enhanced condition of whistler waves. *Geophysical Research Letters*, *40*(17), 4520–4525. https://doi.org/10.1002/grl.50916

Miyoshi, Y., Morioka, A., Kataoka, R., Kasahara, Y., & Mukai, T. (2007). Evolution of the outer radiation belt during the November 1993 storms driven by corotating interaction regions. *Journal of Geophysical Research*, *112*, A05210. https://doi.org/10.1029/2006JA012148

Murphy, K. R., Watt, C. E. J., Mann, I. R., Jonathan Rae, I., Sibeck, D. G., Boyd, A. J., et al. (2018). The global statistical response of the outer radiation belt during geomagnetic storms. *Geophysical Research Letters*, *45*, 3783–3792. https://doi.org/10.1002/2017GL076674

Ozeke, L. G., Mann, I. R., Olifer, L., Dufresne, K. Y., Morley, S. K., Claudepierre, S. G., et al. (2020). Acceleration during the March 2015 and 2013 storms: The role of ultra-low frequency wave transport from a dynamic outer boundary. *Journal of Geophysical Research*, *125*, e2019JA027179. https://doi.org/10.1029/2019JA027179

Perry, K. L., Hudson, M. K., & Elkington, S. R. (2005). Incorporating spectral characteristics of Pc5 waves into three-dimensional radiation belt modeling and the diffusion of relativistic electrons. *Journal of Geophysical Research*, *110*, A03215. https://doi.org/10.1029/2004JA010760

Richardson, I. G., & Cane, H. V. (2012). Solar wind drivers of geomagnetic storms during more than four solar cycles. *Journal of Space Weather and Space Climate*, *2*, A01. https://doi.org/10.1051/swsc/2012001

Richardson, I. G., Webb, D. F., Zhang, J., Berdichevsky, D. B., Biesecker, D. A., Kasper, J. C., et al. (2006). Major geomagnetic storms (Dst ≤−100 nT) generated by corotating interaction regions. *Journal of Geophysical Research*, *111*, A07S09. https://doi.org/10.1029/2005JA011476

Sandhu, J. K., Rae, I. J., Wygant, J. R., Breneman, A. W., Tian, S., Watt, C. E. J., et al. (2021). ULF wave driven radial diffusion during geomagnetic storms: A statistical analysis of Van Allen Probes observations. *Journal of Geophysical Research: Space Physics*, *126*, e2020JA029024. https://doi.org/10.1029/2020JA029024

Schulz, M., & Lanzerotti, L. J. (1974). *Particle Diffusion in the Radiation Belts*. Springer-Verlag.

Sergeev, V. A., Angelopoulos, V., & Nakamura, R. (2012). Recent advances in understanding substorm dynamics. *Geophysical Research Letters*, *39*(5), L05101. https://doi.org/10.1029/2012GL050859

Shprits, Y. Y., & Ni, B. (2009). Dependence of the quasi-linear scattering rates on the wave-normal distribution for chorus waves in the radiation belt. *Journal of Geophysical Research*, *114*, A11205. https://doi.org/10.1029/2009JA014223

Souza, V. M., Lopez, R. E., Jauer, P. R., Sibeck, D. G., Pham, K., Da Silva, L. A., et al. (2017). Acceleration of radiation belt electrons and the role of the average interplanetary magnetic field B_z component in high speed streams. *Journal of Geophysical Research: Space Physics*, *122*, 10084–10101. https://doi.org/10.1002/2017ja024187

Stone, E., Frandsen, A. M., Mewaldt, R. A., Christian, E. R., Margolies, D., Ormes, J. F., & Snow, F. (1998). The advanced Composition Explorer. *Space Science Reviews*, *86*(1/4), 1–22 https://doi.org/10.1023/A:1005082526237

Thorne, R. M. (2010). Radiation belt dynamics: The importance of wave-particle interactions. *Geophysical Research Letters*, *37*, L22107. https://doi.org/10.1029/2010GL044990

Thorne, R. M., Li, W., Ni, B., Ma, Q., Bortnik, J., Chen, L., et al. (2013). Rapid local acceleration of relativistic radiation-belt electrons by magnetospheric chorus. *Nature*, *504*(7480), 411–414. https://doi.org/10.1038/nature12889

Tsurutani, B. T., & Gonzalez, W. D. (1997). The interplanetary causes of magnetic storms: A review in Magnetic Stroms. In B. T. Tsurutani, W. D. Gonzalez, Y. Kamide & J. K. Arballo (Eds.), *Geophys. Monogr. Ser*. (Vol. 98, pp. 77–89). AGU. https://doi.org/10.1029/GM098p0077

Tsurutani, B. T., Gonzalez, W. D., Gonzalez, A. L. C., Tang, F., Arballo, J. K., & Okada, M. (1995). Interplanetary origin of geomagnetic activity in the declining phase of the solar cycle. *Journal of Geophysical Research*, *100*(A11), 21717–21733. https://doi.org/10.1029/95JA01476

Tsurutani, B. T., & Smith, E. J. (1974). Postmidnight chorus: A substorm phenomenon. *Journal of Geophysical Research*, *79*(1), 118–127. https://doi.org/10.1029/JA079i001p00118

Turner, D. L., Kilpua, E. K. J., Hietala, H., Claudepierre, S. G., O'Brien, T. P., Fennell, J. F., et al. (2019). The response of Earth's electron radiation belts to geomagnetic storms: Statistics from the Van Allen Probes era including effects from different storm drivers. *Journal of Geophysical Research: Space Physics*, *124*, 1013–1034. https://doi.org/10.1029/2018JA026066

Turner, N. E., Mitchell, E. J., Knipp, D. J., & Emery, B. A. (2006). Energetics of magnetic storms driven by corotating interaction regions: A study of geoeffectiveness, in Recurrent Magnetic Stroms. In B. T. Tsurutani, R. McPherron, G. Lu, J. H. A. Sobral, & N. Gopalswamy (Eds.), *Geophys. Monogr. Ser*. (Vol. 167, pp. 113–124). AGU. https://doi.org/10.1029/167GM11

Ukhorskiy, A. Y., Sitnov, M. I., Takahashi, K., & Anderson, B. J. (2009). Radial transport of radiation belt electrons due to storm time Pc5 waves. *Annales Geophysicae*, *27*, 2173–2181. https://doi.org/10.5194/angeo-27-2173-2009

Ukhorskiy, A. Y., Takahashi, K., Anderson, B. J., & Korth, H. (2005). Impact of toroidal ULF waves on the outer radiation belt electrons. *Journal of Geophysical Research*, *110*, A10202. https://doi.org/10.1029/2005JA011017

Viljanen, A., & Hakkinen, L. (1997). *Image magnetometer network, in satellite-ground based coordination sourcebook*, In M. Lockwood, M. N. Wild, & H. J. Opgenoorth (Eds.), ESA Publications, p. 111.

Wygant, J. R., Bonnell, J. W., Goetz, K., Ergun, R. E., Mozer, F. S., Bale, S. D., et al. (2013). The electric field and waves instruments on the radiation belt storm probes mission. *Space Science Reviews*, *179*(1–4), 183–220. https://doi.org/10.1007/s11214-013-0013-7

Xiao, F., Su, Z., Zheng, H., & Wang, S. (2010). Three-dimensional simulations of outer radiation belt electron dynamics including cross-diffusion terms. *Journal of Geophysical Research*, *115*, A05216. https://doi.org/10.1029/2009JA014541

Yeoman, T. K., Klimushkin, D. Y., & Mager, P. N. (2010). Intermediate-m ULF waves generated by substorm injection: A case study. *Annales Geophysicae*, *28*, 1499–1509. https://doi.org/10.5194/angeo-28-1499-2010

Zhao, H., Baker, D. N., Li, X., Jaynes, A. N., & Kanekal, S. G. (2018). The acceleration of ultrarelativistic electrons during as mall to moderate storm of 21 April 2017. *Geophysical Research Letters*, *45*, 5818–5825. https://doi.org/10.1029/2018GL078582